Theor. Comput. Fluid Dyn. (2017) 31:447–469
DOI 10.1007/s00162-017-0429-x

ORIGINAL ARTICLE

Alexander Yu. Gelfgat

Time-dependent modeling of oscillatory instability of three-dimensional natural convection of air in a laterally heated cubic box

Received: 18 March 2016 / Accepted: 22 March 2017 / Published online: 4 April 2017

Abstract Transition from steady to oscillatory buoyancy convection of air in a laterally heated cubic box is studied numerically by straight-forward time integration of Boussinesq equations using a series of gradually refined finite volume grids. Horizontal and spanwise cube boundaries are assumed to be either perfectly thermally conducting or perfectly thermally insulated, which results in four different sets of thermal boundary conditions. Critical Grashof numbers are obtained by interpolation of numerically extracted growth/decay rates of oscillation amplitude to zero. Slightly supercritical flow regimes are described by time-averaged flows, snapshots, and spatial distribution of the oscillation amplitude. Possible similarities and dissimilarities with two-dimensional instabilities in laterally heated square cavities are discussed. Break of symmetries and sub- or supercritical character of bifurcations are examined. Three consequent transitions from steady to the oscillatory regime, from the oscillatory to the steady regime, and finally to the oscillatory flow, are found in the case of perfectly insulated horizontal and spanwise boundaries. Arguments for grid and time-step independence of the results are given.

Keywords Natural convection · Instability · Direct numerical simulation

1 Introduction

This study revisits a well-known problem of oscillatory instability of buoyancy convection in a laterally heated cubic cavity. More than a decade ago, a significant effort was invested in the study of instability of convection in laterally heated two-dimensional cavities. Cavities of different aspect ratios and fluids with different Prandtl numbers were taken into consideration. For more details and relevant literature, the reader is referred to the book [1]. It is well known nowadays that the primary instability of steady buoyancy convection flows in laterally heated cavities sets in via a Hopf bifurcation and results in an oscillatory flow regime. It is known also that flows in horizontally or vertically elongated cavities exhibit multiplicity of asymptotically stable steady [2] and oscillatory [3] states. Mathematical and numerical approaches for path-following and stability analysis, especially with respect to fluid dynamics problems, are being developed continuously, see, e.g., reviews [4–6] . While several decades ago the study of stability of a numerically calculated flow was a challenging state-of-the-art computational task, with the development of computational tools and computer power, study of stability or state multiplicity in a two-dimensional flow model became feasible and can be performed by means of several

Communicated by Vassilios Theofilis.

Electronic supplementary material The online version of this article (doi:10.1007/s00162-017-0429-x) contains supplementary material, which is available to authorized users.

A. Yu. Gelfgat (✉)
School of Mechanical Engineering, Faculty of Engineering, Tel-Aviv University, 69978 Ramat Aviv, Tel Aviv, Israel
E-mail: gelfgat@tau.ac.il

numerical tools [6]. The same tools can be applied when the stability of a two-dimensional base flow with respect to three-dimensional perturbations periodic in one spatial direction is studied [3,7]. These problems were defined as Bi-Global linear stability problems in [4,5]. However, it remains challenging when the basic flow is three-dimensional, so that no simplifications such as spatial periodicity assumptions can be made. The latter is defined as the TriGlobal linear stability problem [4,5].

Among a variety of theoretical and applied fully three-dimensional (TriGlobal) problems, two widely accepted benchmark configurations are usually considered. The first one is flow in a lid-driven cubic cavity, for which the primary instability was recently studied, and the results were verified by independent numerical approaches [8–11], as well as validated in an experiment [12]. The second one is linear instability of buoyancy convection of air (assuming the Prandtl number $Pr = 0.71$) in a laterally heated cube. The latter problem was studied experimentally in [13]. Early numerical studies considered perfectly thermally conducting horizontal boundaries of the cube [14,15], as in the above experiment. Later studies focused on a more challenging problem with perfectly thermally insulated horizontal boundaries [16–20]. The spanwise boundaries were taken as perfectly thermally insulated in all the above studies, so that the effect of these boundary conditions was never studied. All above studies were carried out using straight-forward time integration of the three-dimensional Boussinesq equations.

As is known from well-established numerical solutions obtained for the instability of convective air flow in two-dimensional laterally heated square cavities, which is a Bi-Global problem according to [4,5], the critical Grashof number for perfectly thermally conducting horizontal boundaries is of the order of 10^6, while for perfectly thermally insulated borders it becomes larger than 10^8 [2,20,22]. This makes the problem with perfectly thermally conducting boundaries computationally easier, so that 3D results obtained in [14,15] compare rather well with the experimental measurements of [13]. At the same time, the critical parameters obtained for the primary stability of 3D convection in a cube with perfectly thermally insulated horizontal boundaries [16–19] exhibit a noticeable scatter. The main reason for the scatter can be insufficient numerical convergence. Most of the cited works report grid convergence of some parameters of steady-state flows; however, none of them reported how the critical Grashof (Rayleigh) number varies with grid refinement. Grid convergence of the oscillation frequency of a computed slightly supercritical state was reported only in [20].

It already became common knowledge that a numerically accurate solution of a stability problem usually requires finer resolution than computation of a steady flow only. The finer resolution is needed because, along with the steady-state flow, one has to calculate the most unstable eigenmode, which can be more difficult than computation of the flow itself. A classic example of the latter is 2D configuration with thermally insulated horizontal boundaries, in which instability sets in inside very thin boundary layers adjacent to the hot and cold walls [7,21–23]. More results on grid convergence in 2D benchmark problems can be found in [22]. When instability is simulated by a straight-forward time integration, similar questions arise regarding the time-step and time-integration method independence, but, as a rule, are not addressed.

The primary goal of this study was to find critical Grashof numbers at which the steady-state flows lose stability and become oscillatory. Performing computations on the gradually refined grids, having 100^3, 150^3, 200^3, and 256^3 finite volumes, we intended to arrive to converged values of the critical Grashof numbers, as well as to obtain numerically converged critical frequencies of appearing oscillations. Additionally, we obtained new results on the symmetry preservation or breaking in slightly supercritical flows. Also, we make some arguments on the sub- and supercriticality of the bifurcations observed. The most unexpected, and never reported observation, was a cascade of three consequent steady–oscillatory transitions observed in the AA–AA case.

In the present study, the instability onset and slightly supercritical oscillatory regimes of air convection in a cubic laterally heated box are studied by a straight-forward time integration of the Boussinesq equations. To illustrate three-dimensional velocity patterns, we use the method of quasi-two-dimensional divergence-free projections recently proposed in [24,25]. All the boundaries are considered as no-slip. Two opposite vertical boundaries are assumed to be isothermal, while the upper and lower horizontal boundaries are considered either perfectly thermally conducting, or perfectly thermally insulated. Also, the second pair of the opposite vertical boundaries, which we call spanwise boundaries, is assumed to be perfectly conducting or perfectly insulated. Thus, four sets of different thermal boundary conditions are taken into consideration. This extends the benchmark data for future 3D stability studies and offers to consider two "easier" cases with the perfectly conducting horizontal boundaries, as well as two "difficult" cases defining the horizontal boundaries as thermally insulated. Together with the results on lid-driven cubic cavity [8–11], these form a quite representative set of three-dimensional stability benchmark problems.

We are aware that pseudo-spectral and collocation methods may yield better accuracy for model problems in simple geometries, as those considered here. At the same time, we are interested in the three-dimensional

modeling and stability analysis of more complicated flows developing inside and around bodies of arbitrary shape. Besides a wide set of curved-boundary-fitted numerical methods, the latter can be achieved by combining of the fixed grid finite volume approach used below with the immersed boundary technique, as it was done recently in [26]. Our most representative 256^3 nodes grid is slightly finer than those used in the recent studies of the primary instability in the lid-driven cavity [8–11], where the finest grid had only 200^3 nodes.

In the following, we present a brief formulation of the problem (Sect. 2) and describe two independent time-integration techniques applied (Sect. 3). In Sect. 4, we briefly describe the test calculations and the technique used for visualization of the three-dimensional velocity field. Results on transition to unsteadiness with the necessary discussion are presented in Sect. 5. Conclusions followed by a short discussion are summarized in Sect. 6.

2 Formulation of the problem

We consider natural convection of an incompressible fluid in a cubic cavity, whose opposite sidewalls are kept at constant and different temperatures T_{hot} and T_{cold}. The flow is described by a set of Boussinesq equations that are rendered dimensionless taking the cube side length H as a characteristic scale, and H^2/ν, ν/H, and $\rho\nu^2/H^2$ as scales of the time t, the velocity $\boldsymbol{v} = (u, v, w)$ and the pressure p, respectively. Here, ν is the fluid kinematic viscosity and ρ is the density. The temperature is rescaled to a dimensionless function using the relation $T \to (T - T_{\text{cold}}) / (T_{\text{hot}} - T_{\text{cold}})$. Additionally, the dimensionless time, velocity, and pressure are scaled, respectively by $Gr^{-1/2}$, $Gr^{1/2}$, and Gr, where $Gr = g\beta (T_{\text{hot}} - T_{\text{cold}}) H^3/\nu^2$ is the Grashof number, g is the gravity acceleration and β is the thermal expansion coefficient. The resulting system of momentum, energy, and continuity equations is defined in a cube $0 \le x, y, z \le 1$ and reads

$$\frac{\partial T}{\partial t} + (\boldsymbol{v} \cdot \nabla) T = \frac{1}{Pr Gr^{1/2}} \Delta T \tag{1}$$

$$\frac{\partial \boldsymbol{v}}{\partial t} + (\boldsymbol{v} \cdot \nabla) \boldsymbol{v} = -\nabla p + \frac{1}{Gr^{1/2}} \Delta \boldsymbol{v} + T \boldsymbol{e}_z \tag{2}$$

$$\nabla \cdot \boldsymbol{v} = 0. \tag{3}$$

Here $Pr = \nu/\alpha$ is the Prandtl number, and α is the thermal expansion coefficient. All the boundaries are assumed to be no-slip. Two vertical boundaries at $x = 0, 1$ are kept isothermal, so that

$$T(x = 0, y, z) = 1, \quad T(x = 1, y, z) = 0. \tag{4}$$

Other boundaries are assumed to be either perfectly thermally conducting or perfectly thermally insulated. Following the notations introduced in [27] we denote a pair of perfectly insulated (adiabatic) boundaries as AA, and a pair of perfectly conducting boundaries as CC. The four sets of thermal boundary conditions considered below are

$$\text{CC–CC}: T(x, y = 0, z) = T(x, y = 1, z) = T(x, y, z = 0) = T(x, y, z = 1) = 1 - x \tag{5}$$

$$\text{CC–AA}: T(x, y = 0, z) = T(x, y = 1, z) = 1 - x, \left(\frac{\partial T}{\partial z}\right)_{z=0} = \left(\frac{\partial T}{\partial z}\right)_{z=1} = 0 \tag{6}$$

$$\text{AA–CC}: \left(\frac{\partial T}{\partial y}\right)_{y=0} = \left(\frac{\partial T}{\partial y}\right)_{y=1} = 0, T(x, y, z = 0) = T(x, y, z = 1) = 1 - x \tag{7}$$

$$\text{AA–AA}: \left(\frac{\partial T}{\partial y}\right)_{y=0} = \left(\frac{\partial T}{\partial y}\right)_{y=1} = 0, \left(\frac{\partial T}{\partial z}\right)_{z=0} = \left(\frac{\partial T}{\partial z}\right)_{z=1} = 0. \tag{8}$$

As is noted in [17], the problem has three symmetries: (i) reflection symmetry with respect to the midplane $y = 0.5$, $\{u, v, w, \theta\}(x, y, z) = \{u, -v, w, \theta\}(x, 1 - y, z)$, (ii) 2D rotational symmetry with respect to rotation in 180° around the line $x = z = 0.5$, $\{u, v, w, \theta\}(x, y, z) = -\{u, -v, w, \theta\}(1 - x, y, 1 - z)$ and (iii) 3D centro-symmetry $\{u, v, w, \theta\}(x, y, z) = -\{u, v, w, \theta\}(1 - x, 1 - y, 1 - z)$. Here $\theta = T - (1 - x)$. These symmetries are characteristic for steady-state flows, however, can be broken by instability, so that supercritical oscillatory flows can maintain only one of them or be fully non-symmetric. Clearly, the centro-symmetry (iii) is a superposition of the two other symmetries, so that seemingly it cannot be preserved if one of the symmetries (i) or (ii) is broken. However, there exists an exceptional case. Assume that both symmetries (i)

and (ii) are broken. Then, the coordinate transformations in (i) and (ii) can be presented as a sum of symmetric and antisymmetric parts. If the antisymmetric parts of (i) and (ii) cancel each other, the 3D centro-symmetry (iii) persists. We follow the above symmetries by examination of the maximal absolute difference of the values of θ in the points of symmetry. In particular, we observe the above exceptional case in the AA–CC configuration (see below).

To compare results with the corresponding two-dimensional model of buoyancy convection in a square cavity, in the following we call areas adjacent to the cube edges $(0, y, 0)$, $(0, y, 1)$, $(1, y, 0)$, and $(1, y, 1)$ as lower left, upper left, lower right, and upper right corners, respectively.

The primary goal of the $Gr^{1/2}$ scaling is to make the velocity values of the order of unity, which allows for more accurate calculations. The form of Eqs. (1) and (2) shows also that $Gr^{1/2}$ yields an estimate of the Reynolds number, as is known for natural convection flows (see e.g., [28]). As was shown in [29], the same scale is applied to the vertical velocity in the boundary layers developing near vertical heated walls. Also, as is shown in [30], in the CC–AA case, the Brunt–Väisälä frequency is estimated also by $\sqrt{g\beta\,(T_{\rm hot}-T_{\rm cold})\,H}/H$, so that its dimensionless value obtained using the viscous time scale H^2/ν is $\sqrt{g\beta\,(T_{\rm hot}-T_{\rm cold})\,H^3/\nu^2}=Gr^{1/2}$. Thus, the dimensionless time is scaled additionally by the inverse Brunt–Väisälä frequency.

3 Numerical method

The problem is solved using standard finite volume discretization on staggered grids. The resulting schemes yield the second-order approximation in space, and conserve mass, momentum, and internal energy. The scheme conservative properties are considered as a necessary condition for correct numerical identification of the instability threshold. The details are given in [31]. The size of a stretched finite volume grid varies from 100^3 to 256^3. The stretching is the same as in [22]. To generate initial flow close to the asymptotic steady or oscillatory state, the solutions on the coarser grids were interpolated onto the finer grids using the 3D Lagrange interpolation polynomial of the first order.

For the time integration, we apply the same second-order backward scheme and two independent pressure/velocity segregated or coupled approaches. The first one is a fractional step method with the second-order discretization of the time derivative. This scheme is similar to the one applied in [14,15] and is briefly described below. Denoting the time step by δt and by the superscript (n) the function values at $t=n\delta t$, we perform the time integration as

$$\frac{1}{2\delta t}\left(3T^{(n+1)}-4T^{(n)}+T^{(n-1)}\right)+\left(\boldsymbol{v}^{(n)}\cdot\nabla\right)T^{(n)}=\frac{1}{PrGr^{1/2}}\Delta T^{(n+1)} \tag{9}$$

$$\frac{1}{2\delta t}\left(3\boldsymbol{v}^{(n+1/2)}-4\boldsymbol{v}^{(n)}+\boldsymbol{v}^{(n-1)}\right)+\left(\boldsymbol{v}^{(n)}\cdot\nabla\right)\boldsymbol{v}^{(n)}=-\nabla p^{(n)}+\frac{1}{Gr^{1/2}}\Delta\boldsymbol{v}^{(n+1/2)}+T^{(n+1)}\boldsymbol{e}_z \tag{10}$$

$$\Delta\,(\delta p)=\frac{3}{2\delta t}\mathrm{div}\boldsymbol{v}^{(n+1/2)} \tag{11}$$

$$p^{(n+1)}=p^{(n)}+\delta p,\ \boldsymbol{v}^{(n+1)}=\boldsymbol{v}^{(n+1/2)}-\frac{2\delta t}{3}\mathrm{grad}\,(\delta p)\,. \tag{12}$$

First, we compute $T^{(n+1)}$ using Eq. (9), and $\boldsymbol{v}^{(n+1/2)}$ from Eq. (10). Then we calculate the pressure correction from the Poisson equation (11), which is supplied by the Neumann boundary conditions for the pressure. Finally, pressure and velocity are updated according to Eq. (12). Note that the 3/2 coefficient in Eq. (11) follows from the second-order time discretization of the momentum equation (10). A correct solution of Eq. (10) for the pressure correction zeroes the grid divergence of $\boldsymbol{v}^{(n+1)}$ in Eq. (12). Performing one time step requires the solution of one Helmholtz equation for the temperature, three Helmholtz equations for the velocity components, and one Poisson equation for the pressure.

The discretized Helmholtz and Laplace operators are inversed by the direct TPT method [32], which combines the eigenvalue decomposition of an operator with the Thomas algorithm. This direct method is shown to consume less computational time than the standard Krylov-subspace or multigrid iteration techniques when large Reynolds (Grashof) number flows are being calculated on fine grids [32]. Furthermore, since the method used for the Laplacian inverse in Eq. (11) is direct, it yields the solution within the machine accuracy. Formulation of the present numerical schemes ensures that the consecutive action of the grid gradient and divergence result in the grid Laplacian. Altogether, these guarantee that the correction step (12) brings the grid divergence values to machine zero (see [25] for a mathematical proof). In the computations below the maximal absolute grid divergence value was always below 10^{-14}.

The above splitting method is $O\left(\delta t^2\right)$ for velocity, as is proved in [33]. However, it is argued in [34] that owing to Eqs. (11) and (12), the numerical error in the continuity equation $\nabla \cdot \boldsymbol{v} = 0$ is of the order of δt. In the current computations, however, the values of δp and grad (δp) are computed to within the machine precision, so that the error term proportional to δt vanishes. Therefore, the resulting time discretization scheme is $O\left(\delta t^2\right)$ also for velocity divergence.

The second method used for time integration applies the same second-order discretization in the time and pressure/velocity coupled Uzawa-like scheme proposed in [32]. This approach is based on the LU decomposition of the Stokes operator

$$\begin{bmatrix} H_u & 0 & 0 & -\nabla_p^x \\ 0 & H_v & 0 & -\nabla_p^y \\ 0 & 0 & H_w & -\nabla_p^z \\ \nabla_u^x & \nabla_v^y & \nabla_w^z & 0 \end{bmatrix} = \begin{bmatrix} I & 0 & 0 & 0 \\ 0 & I & 0 & 0 \\ 0 & 0 & I & 0 \\ \nabla_u^x H_u^{-1} & \nabla_v^y H_v^{-1} & \nabla_w^z H_w^{-1} & I \end{bmatrix} \begin{bmatrix} H_u & 0 & 0 & -\nabla_p^x \\ 0 & H_v & 0 & -\nabla_p^y \\ 0 & 0 & H_w & -\nabla_p^z \\ 0 & 0 & 0 & C \end{bmatrix}, \tag{13}$$

$$C = \nabla_u^x H_u^{-1} \nabla_p^x + \nabla_v^y H_v^{-1} \nabla_p^y + \nabla_w^z H_w^{-1} \nabla_p^z. \tag{14}$$

Here ∇^x, ∇^y, and ∇^z are the first derivatives in the $x-$, $y-$, and $z-$ directions, and $H = Gr^{-1/2}\Delta - \frac{3}{2\delta t} I$ are the Helmholtz operators, Δ is the Laplacian operator, I is the identity operator and δt is the time step. As above, the coefficient 3/2 follows from discretization of the time derivative. The lower indices show on which variable an operator acts, so that differences of the staggered grids, as well as possible different boundary conditions for different velocity components, can be taken into account. The left hand side is a 4×4 operator matrix that assembles the 3D Stokes operator. The matrix C is generalization of the Uzawa matrix. Unlike the Uzawa matrix, C is not necessarily symmetric and not necessarily positive semi defined [32]. For this time-integration technique, the energy equation (9) is treated as above in Eq. (9), so that at each time step $T^{(n+1)}$ is computed first. The semi-implicit time step for the momentum and continuity equations is reduced to the solution of the linear equations system

$$\begin{bmatrix} H_u & 0 & 0 & -\nabla_p^x \\ 0 & H_v & 0 & -\nabla_p^y \\ 0 & 0 & H_w & -\nabla_p^z \\ \nabla_u^x & \nabla_v^y & \nabla_w^z & 0 \end{bmatrix} \begin{bmatrix} u^{(n+1)} \\ v^{(n+1)} \\ w^{(n+1)} \\ p^{(n+1)} \end{bmatrix} = \begin{bmatrix} R_u \\ R_v \\ R_w \\ 0 \end{bmatrix}. \tag{15}$$

where the right hand sides R contain the non-linear terms and all other terms that are treated explicitly. Using the LU decomposition (13), the solution is obtained in three steps:

1. Solve $\hat{u} = H_u^{-1} R_u$, $\hat{v} = H_v^{-1} R_v$ and $\hat{w} = H_w^{-1} R_v$ for $\hat{u}$, $\hat{v}$ and $\hat{w}$.
2. Solve $p^{(n+1)} = -C^{-1}\left(\nabla_u^x \hat{u} + \nabla_v^y \hat{v} + \nabla_w^z \hat{w}\right)$ for $p^{(n+1)}$.
3. Solve $u^{(n+1)} = \hat{u} + H_u^{-1} \nabla_p^x p^{(n+1)}$, $v^{(n+1)} = \hat{v} + H_v^{-1} \nabla_p^y p^{(n+1)}$, and $w^{(n+1)} = \hat{w} + H_w^{-1} \nabla_p^z p^{(n+1)}$.

(16)

Thus, carrying out of a single time step requires 6 inverses of the Helmholtz operator and one inverse of the pressure matrix C. It is worth noting that in this approach the pressure is defined only at the nodes lying inside the flow region (not boundary nodes), so that no pressure boundary conditions are needed. In the following, the Helmholtz operators are inversed using the TPT method. Inverse of the matrix C requires use of an iterative method. Our numerical experiments showed that the fastest convergence is obtained using the ORTHOMIN(2) method [35]. It is worth mentioning that the first stages of the two time-integration approaches are identical, so that the vectors $\boldsymbol{v}^{(n+1/2)}$ obtained from Eq. (10) coincide with the vectors $\left(\hat{u}, \hat{v}, \hat{w}\right)$ calculated at the first stage of the algorithm (16).

4 Test calculations and visualization technique

At the preliminary stage of test calculations, it was ensured that both time-integration techniques described above arrive to the same steady-state flow at subcritical Grashof numbers. These steady flows coincide with those obtained in [36] using a multigrid pressure-velocity coupling technique for the same finite volume discretization in space. These flows were successfully compared in [36] with other independent results obtained by a collocation method [37], and different lower-order techniques [38–40]. In this section, we focus on the grid convergence of the calculated slightly supercritical oscillatory flows, as well as to establish that two independent

Table 1 Grid convergence of the average values and amplitudes of the total kinetic energy and the Nusselt Number for two characteristic cases illustrated in Fig. 1

Grid	CC–CC case, $Gr = 3.4 \times 10^6$				AA–CC case, $Gr = 1.3 \times 10^8$			
	$\bar{E}_{\rm kin}$	$\overline{Nu}$	$A\,(E_{\rm kin})$	$A\,(Nu)$	$\bar{E}_{\rm kin}$	$\overline{Nu}$	$A\,(E_{\rm kin})$	$A\,(Nu)$
100^3	6.6949×10^{-3}	7.59988	6.306×10^{-5}	0.1935	2.12696×10^{-3}	26.84067	6.453×10^{-6}	9.074×10^{-3}
150^3	6.6968×10^{-3}	7.59804	5.898×10^{-5}	0.1889	2.12490×10^{-3}	26.7625	6.024×10^{-6}	9.944×10^{-3}
200^3	6.6976×10^{-3}	7.59686	5.751×10^{-5}	0.1810	2.12392×10^{-3}	26.7365	9.595×10^{-6}	2.260×10^{-2}
256^3	6.6979×10^{-3}	7.59646	5.681×10^{-5}	0.1793	2.12389×10^{-3}	26.7231	1.093×10^{-5}	2.614×10^{-2}

time-integration techniques arrive to the same asymptotic oscillatory states. Visualization of three-dimensional velocity patterns is discussed in the next section.

The grid convergence is established by comparison with the time histories of the total flow kinetic energy $E_{\rm kin}$ and Nusselt number Nu at the heated wall. The convergence of their average values and amplitudes is reported in Table 1. The calculations were performed with the dimensionless time step 0.002 and remained unchanged when it was decreased to 0.001. Based on this, we assume the time-step independence of the results and use $\delta t = 0.002$ for all the further calculations. Note that studies [14,15] reported time-step independence of the results starting from $\delta t = 1/16 = 0.0625$. Our numerical experiments show that this time step is too large for accurate computation of the critical parameters. Thus, for the CC–AA case, computations with $\delta t = 0.01$ yield $Gr_{\rm cr} = 2.99 \times 10^6$. Reduction in the time step in ten times yields $Gr_{\rm cr} = 3.30 \times 10^6$, which already seems to be time-step independent. It is noteworthy that the oscillation frequency slightly above the critical point is 0.266 and 0.264 for the two above computations, respectively. The latter close values show that the frequency scales with the $\sqrt{Gr}$; however, there is no good agreement between the two results if their dimensional values are considered. Note also, that the time step in similar time-dependent calculations [19] was 5×10^{-4}, which is consistent with the current study.

A comparison of the oscillatory regimes at $Gr = 3.4 \times 10^6$ in the CC–AA case computed at different grids shows that they become visually indistinguishable starting from the 150^3 grid. The oscillations at the 100^3 grid slightly deviate at the minimal $E_{\rm kin}$ and Nu values. The corresponding rows of Table 1 show that $E_{\rm kin}$ and Nu average values converge up to the fourth significant digit, while for the oscillation amplitudes we can expect convergence within two first decimal places.

The case of thermally insulated horizontal boundaries is significantly more challenging, because the boundary conditions allow for development of thin boundary layers along the vertical walls and the critical Grashof number becomes two orders of magnitude larger than that for the perfectly conducting horizontal boundaries [2,7,21]. Thus, the results at $Gr = 1.3 \times 10^8$ in the AA–CC case still remain slightly different for 200^3 and 256^3 grids, so that we cannot expect a complete convergence of the critical parameters there. The last four rows of Table 1 show that in spite of a noticeably larger Grashof number, the oscillation amplitudes are an order of magnitude smaller than in the previous case. This indicates additionally on the computational difficulties arising in the case of thermally insulated horizontal boundaries. The amplitudes convergence in the considered case is non-monotonic, and only the first decimal place is expected to be converged for the finest 256^3 grid. At the same time, the average values, as in the previous case, converge within the forth decimal place.

Results yielded by the pressure / velocity coupled and segregated solvers were compared for two-frequency oscillatory regime at quite a large Grashof number $Gr = 3 \times 10^8$ for the AA–AA case (see below). This comparison showed that two independent solvers arrive to the same oscillatory regimes, so that oscillating dependencies of the total kinetic energy and the Nusselt number (see below) coincide within five decimal places. This allowed us to rely on results obtained by the faster pressure / velocity segregated solver.

The three-dimensional temperature field can be easily represented by its isosurfaces. Visualization of three-dimensional velocity fields is a considerably more complicated task. In the present study, we implement the visualization method proposed in [24,25], making divergence-free projections of velocity on three sets of coordinate planes, (x, y), (y, z), and (x, z). Namely, we compute three projections $\boldsymbol{v}_1, \boldsymbol{v}_2, \boldsymbol{v}_3$ of the velocity field $\boldsymbol{v}$ on subspaces formed by divergence-free velocity fields having only two non-zero components in the coordinate directions. This allows us to visualize 3D flow by isosurfaces of the three scalar functions Ψ_x,Ψ_y, and Ψ_z, which are non-zero components of vector potentials of the above projections. The projection vectors are tangent to the isosurfaces, so that visualization of a divergence-free three-dimensional flow can be done by three independent frames depicting the vector potentials and the velocity projections (see [24,25] for details).

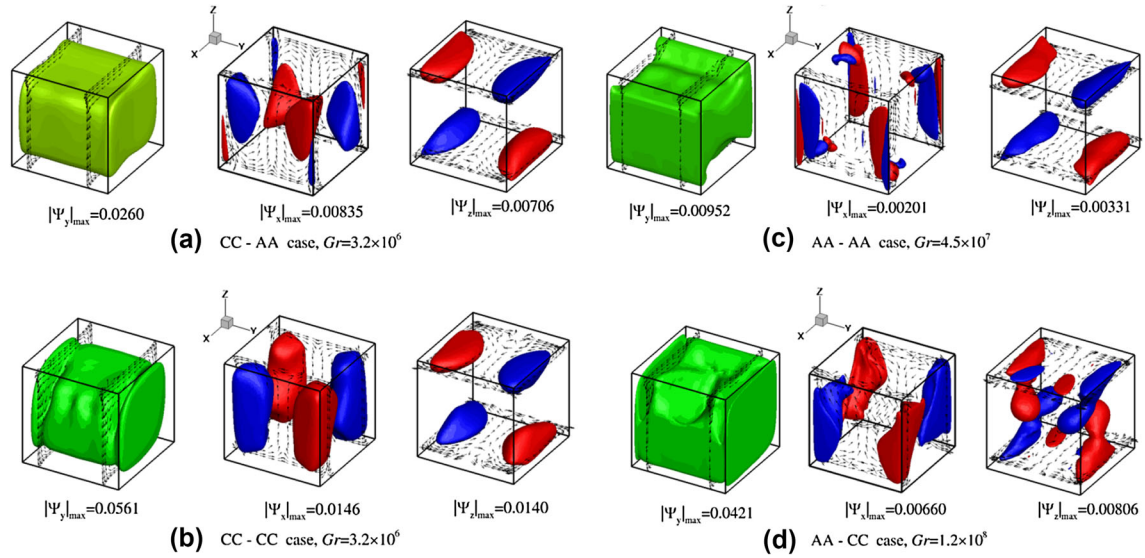

Fig. 1 Visualization of 3D velocity fields corresponding to slightly subcritical steady states. Divergence-free projections of velocity fields on the coordinate planes are shown by vectors. Isosurfaces of the velocity potentials, to which the vector fields are tangent, are shown by *colors*. In the frames **a**–**c**, the potential isosurfaces are plotted for the levels of 0.3 multiplied by the corresponding maximal absolute value. In the frame **d**, the factors are 0.5, 0.3, and 0.4 for Ψ_y, Ψ_x, and Ψ_z, respectively (color figure online)

Examples of this visualization showing three vector potentials, together with the divergent-free velocity projections (depicted by arrows) on the corresponding coordinate planes are presented in Fig. 1. It is clearly seen that the divergence-free velocity projection vectors are tangent to the isosurfaces of the vector potentials. It should be noticed also that projections on the (x, z) planes (left frames in Fig. 1a-d) correspond to two-dimensional convective circulations altered by the three-dimensional effects. The comparison of 2D and 3D velocity patterns for the AA–AA case is reported in [24]. The three-dimensional effects are rather clearly seen from two other frames. The flow contains two pairs of diagonally symmetric rolls in the (y, z) planes (middle frames), and two other diagonally symmetric rolls in the (x, y) planes (right frames). Owing to motion along these rolls, the main circulation depicted in the two right frames deviates from its two-dimensional counterpart. As is shown in [24], the deviation increases with the increase in the Grashof (or Rayleigh) number. Below, we use this approach to visualize steady, time-averaged, and time-dependent flows.

5 Transition to unsteadiness

A straight-forward way to find a critical Grashof number from a series of time-dependent computations is extraction of growth or decay rates from the time histories, followed by the interpolation of growth rates to the zero value. This approach assumes that the single-frequency oscillation amplitude monotonically grows or decays in time. In these cases, assuming a supercritical bifurcation, the critical Grashof number is obtained by a linear interpolation between the two closest to zero, negative, and positive growth rates. If the bifurcation is found to be subcritical, the extrapolation to zero is done using the two smallest decay rates. In some cases, we observed two-frequency oscillatory regimes with amplitudes of either frequencies decaying, or one of them growing. To ensure correct results also for these cases, we follow [9] and apply a non-linear least square fit that approximates a two-frequency signal, from which we extract growth/decay rates of each of the harmonics.

Also, as will be clear from the results below, it is essential to ensure that computations converge to a steady state, so that a slowly developing transient regime will not be mistakenly interpreted as a stationary state. Here, the computations process was terminated after the pointwise relative difference between all the variables at two consecutive time steps was below 10^{-9}.

The results of interpolating of all the growth rates to zero and the resulting critical Grashof numbers are reported in Table 2. The corresponding oscillation frequencies are given in Table 3. The results in Tables 2 and 3 are compared with the experiment [13], and the numerically converged 2D result of [22] obtained on a 400^2 grid, and several independent three-dimensional numerical results.

Table 2 Estimation of the critical Grashof number for buoyancy convection in a laterally heated cube from time-dependent runs

Case	100^3	150^3	200^3	256^3	[1, 2], 120^3 FV grid	[3] 61^3 collocation points	[4] 60^3 grid
CC–CC	3.32×10^6	3.33×10^6	3.33×10^6	3.33×10^6			
CC–AA	3.29×10^6	3.29×10^6	3.30×10^6	3.30×10^6	3.17×10^6		
AA–CC	1.28×10^8	1.28×10^8	1.19×10^8	1.24×10^8			
AA–AA	4.45×10^7	4.40×10^7	4.59×10^7	4.58×10^7		4.51×10^7	4.46×10^7
AA–AA	6.62×10^7	6.95×10^7	7.12×10^7	7.2×10^7			
AA–AA	2.33×10^8	2.76×10^8	2.80×10^8	2.80×10^8			
Case	[5] 120^3 grid	[6] 81^3 FD grid	[7] 80^3 collocation points	[8] Experiment	[9] 2D problem 400^2 FV grid		
CC–CC				4.5×10^6	2.97×10^6		
CC–AA					2.97×10^6		
AA–CC					2.57×10^8		
AA–AA			$(4.4-4.9) \times 10^7$				
AA–AA							
AA–AA	$(3.5-5.6) \times 10^8$	1.73×10^8			2.57×10^8		

References: [1] Janssen et al. [14]; [2] Janssen and Henkes [15]; [3] Labrosse et al. [16]; [4] De Gassowski et al. [17]; [5] Janssen and Henkes [20]; [6] Sheu and Lin [18]; [7] Soucasse et al. [19]; [8] Jones and Briggs [13]; [9] Gelfgat [22]

Table 3 Estimation of the oscillation frequency for buoyancy convection in a laterally heated cube from time-dependent runs. References are same as for Table 2

Case	100^3	150^3	200^3	256^3	[1, 2], 120^3 FV grid	[3] 61^3 collocation points	[4] 60^3 grid	[5] 120^3 grid
CC–CC	0.281	0.282	0.282	0.282				
CC–AA	0.263	0.264	0.264	0.264	0.266			
AA–CC	0.157	0.00990	0.00990	0.00989				
AA–AA	0.0174	0.0105	0.0105	0.0107		0.009	0.0062	
AA–AA	0.106	0.104	0.105	0.105				
AA–AA	0.0149	0.522	0.525	0.525				0.532
Case	[6] 81^3 FD grid	[7] 80^3 collocation points	[8] Experiment	[9] 2D problem 400^2 FV grid				
CC–CC			0.26	0.254				
CC–AA				0.254				
AA–CC				0.05522				
AA–AA		0.00795						
AA–AA								
AA–AA	0.3			0.05522				

The cases with thermally insulated horizontal boundaries (AA–AA and AA–CC) are considerably more complicated and computationally challenging. Note the obvious scatter in the earlier results, obtained on coarser grids, reported in Tables 2 and 3. In all previous studies, the number of grid or collocation nodes in one spatial direction did not exceed 100, which can be insufficient already for resolving thin thermal boundary layers adjacent to the cold and hot walls in a laterally heated two-dimensional square cavity. Also, in the present calculations, we obtain qualitatively correct steady–oscillatory transitions only starting from a 150^3 grid. Calculations on a 100^3 grid sometimes yield inaccurate frequency since the most unstable perturbation is not yet resolved numerically. We assume that insufficient spatial resolution is the main reason for disagreement in the previous results.

Flow time histories are monitored by storing the values of dimensionless total kinetic energy E_{kin} and the Nusselt number Nu at the cold wall, which are defined as

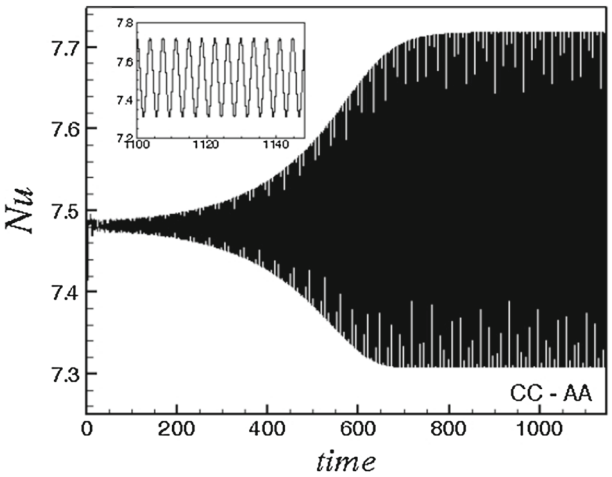

Fig. 2 Time evolution of the total kinetic energy and the Nusselt number from $Gr = 3.4 \times 10^6$ to $Gr = 3.5 \times 10^6$. CC–AA case. Calculation on the 100^3 grid

$$E_{\text{kin}} = \frac{1}{2} \int_V \left(u^2 + v^2 + w^2\right) \mathrm{d}V \tag{17}$$

$$Nu = \int_0^1 \int_0^1 \left[\frac{\partial T}{\partial x}\right]_{x=0} \mathrm{d}y\mathrm{d}z - 1. \tag{18}$$

In Eq. (18), we subtract the Nusselt number of the purely conducting state, which is exactly a unity, in order to observe the convective flow effect only. Note also that the dimensionless values of E_{kin} are scaled by Gr^{-1}, so its scaled value usually decreases with the growth of Gr.

Since all the oscillatory flows computed at small supercriticalities are periodic, the corresponding average flows can be easily calculated by integration over a single period. At the same time, since the oscillation frequency ω is already known via the Fourier analysis of the time dependencies of the total kinetic energy and the Nusselt number, additional time integration over a period can be performed together with evaluation of the Fourier integral

$$\{A_u, A_v, A_w, A_T\}_{ijk} = \frac{\omega}{\pi} \int_0^{2\pi/\omega} \{u, v, w, T\}_{ijk} \, \mathrm{e}^{-i\omega t} \mathrm{d}t \tag{19}$$

where A with a subscript stays for the amplitude of the corresponding function oscillations with the frequency ω, and the integral is performed at each grid point. The three-dimensional amplitude functions describe the spatial pattern of the oscillation amplitude for each scalar function. When the bifurcation is supercritical and supercriticality is small, they also represent patterns of the most linearly unstable disturbance. In the following, we use the absolute value of A_T to illustrate calculated oscillatory regimes.

The slightly supercritical oscillatory flows are visualized by snapshots of the vector potentials described in [24,25]. Animations of the oscillatory regimes described below are supplied as separate files and are reported as 3D snapshots. We also tried to compare time-averaged flow patterns with those of the steady states. Steady states at the supercritical Grashof numbers were calculated by the Newton method using the approach of [37] with the large-time-step iterations performed, as proposed in [32].

5.1 CC–CC and CC–AA cases

The steady–oscillatory transition seems to be similar: In both cases, the exponential amplitude growth is followed by a transition to another oscillatory regime (see below). An example of the amplitude growth and further non-linear evolution of the flow oscillations for the CC–AA case is illustrated in Fig. 2.

As follows from Table 2, in both CC–CC and CC–AA cases, the critical Grashof number and the critical frequency are almost independent on the spanwise boundary conditions. The obtained value of $Gr_{\text{cr}} \approx 3.3 \times 10^6$ is well compared with the two-dimensional one, as well as with the results of [14,15], however, is noticeably lower than the experimentally observed value 4.5×10^6 of [13]. The discrepancy can be caused, for example,

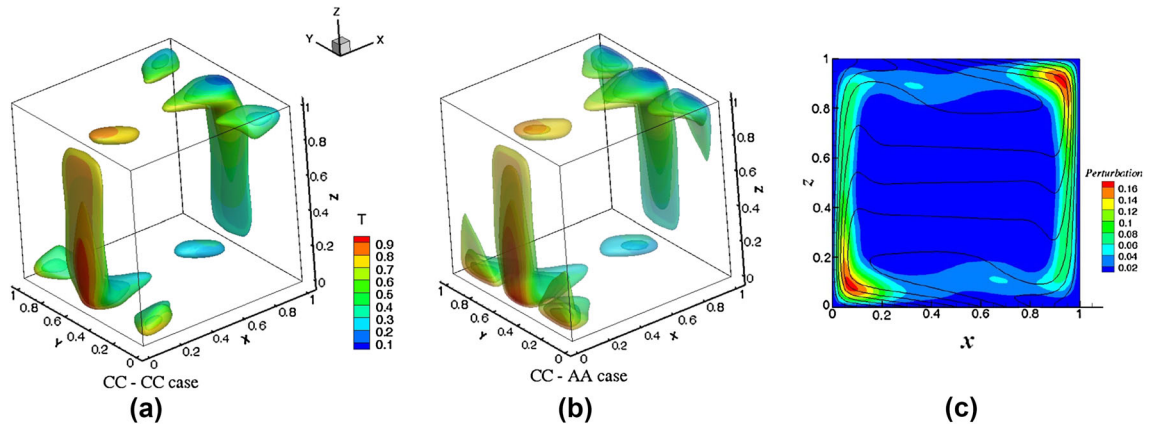

Fig. 3 Amplitude of temperature oscillations at $Gr = 3.4 \times 10^6$ in the CC–CC (**a**) and CC–AA (**b**) cases. *Colors* of the isosurfaces correspond to the average temperature values. **c** Isotherms (*black lines*) and amplitude of the most unstable temperature perturbation (*colors*) in the 2D case with perfectly conducting horizontal boundaries. Calculation on the 100^3 grid. Maximal values of the amplitude and the levels plotted are, respectively, 0.0769, 0.01, 0.02, 0.03 in the frame **a** and 0.114, 0.015, 0.025, 0.035 in the frame **b** (color figure online)

by imperfections of experimental boundary conditions, or by sensitivity of thermocouples that could measure temperature oscillations starting from the rather large amplitude. The frequencies are well compared with the two-dimensional prediction and are close to the experimentally measured one.

The amplitude of the temperature oscillations at $Gr = 3.4 \times 10^6$ is shown in Fig. 3a, b for the CC–CC and CC–AA cases, respectively. The amplitude isosurfaces are colored by values of the time-averaged temperature at the same points. Both amplitude patterns are similar. We observe that the maximal amplitudes are located in the lower left and upper right corners of the midplane $y = 0.5$. Note that in the lower left corner, the hot fluid is located below the cold one, while in the upper right corner the cold fluid is located above the hot one, as is indicated by the colors. This observation was made previously in [14,15], where it was argued that the instability is caused by the Rayleigh-Bénard mechanism. Figure 3c shows isotherms and distribution of the amplitude of the most unstable perturbation obtained by the linear stability analysis [7,22] for the two-dimensional CC case. Comparison with the 3D result, which must be done in the midplane $y = 0.5$, shows that in the 2D configuration we observe a similar pattern of the amplitude with the maxima located in the lower left and upper right corners. Taking into account close critical Grashof numbers and critical frequencies (Tables 2, 3), we conclude that in these cases the 2D model correctly describes the instability onset, which takes place due to the Rayleigh-Bénard mechanism.

Comparing the subcritical steady states at $Gr = 3.2 \times 10^6$ (Fig. 1a, b), we observe that in the CC–CC case the flow is more intensive. The latter follows from comparison of maximal values of the vector potentials that can be interpreted as extended stream functions. Comparison of the maximal velocity values yields for v_x, v_y, and v_z, respectively, 0.251, 0.107, and 0.371 in the CC–CC case; and 0.228, 0.0563, and 0.342 in the CC–AA case. Apparently, this difference in flow intensities is caused by different temperature distribution near the spanwise boundaries (Fig. 3) and, surprisingly, does not affect the instability threshold, which is entirely two-dimensional, so that the most intensive disturbances are located near the $y = 0.5$ midplane. However, it affects further instability development. Thus, examination of slightly supercritical flows at $Gr = 3.4 \times 10^6$ shows that the oscillatory flow in the CC–CC case preserves the reflection symmetry, while 2D rotational symmetry and centro-symmetry are broken. In the CC–AA case, all the three symmetries are broken at $Gr = 3.4 \times 10^6$. Note that the 2D instability sets in with the break of rotation symmetry, which follows from the rotation-antisymmetric pattern of its most unstable perturbation, whose absolute value is shown in Fig. 3c [7]. Thus, the break of rotation symmetry is another similarity between 2D and 3D models with perfectly conducting horizontal boundaries.

If the steady–oscillatory transition takes place via a supercritical Hopf bifurcation and results into a stable limit cycle, the time-averaged flow remains close to the unstable steady state one (see e.g., [41]). Comparison of the total kinetic energy and the Nusselt number of unstable steady state and oscillatory flows at $Gr = 3.4 \times 10^6$ results in the following. In the CC–CC case $E_{\rm kin} = 6.666 \times 10^{-3}$ and 6.669×10^{-3}, $Nu = 7.591$ and 7.600, for the steady and oscillatory states, respectively. In the CC–AA case, the same comparison yields $E_{\rm kin} = 4.796 \times 10^{-3}$ and 4.890×10^{-3}, $Nu = 7.481$ and 7.514. Thus, these two integral characteristics

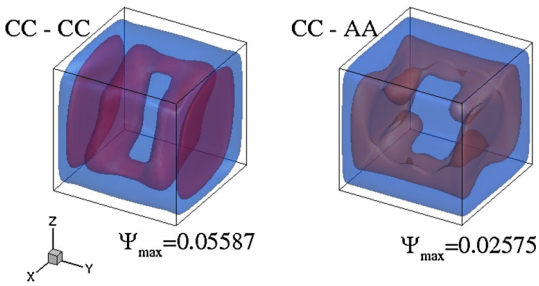

Fig. 4 Patterns of unstable steady-state flows at $Gr = 3.4 \times 10^6$. The plotted levels are 0.00335 and 0.0223 for the CC–CC case and 0.0015 and 0.0195 for the CC–AA case. Calculation on the 100^3 grid. Animation1. Animation2

remain close in both cases, which allows us to assume that we observe supercritical Hopf bifurcations resulting in stable limit cycles. A larger difference in the CC–AA case can be due to steeper increase in the growth rate with the growth of the Grashof number.

The time-averaged flow patterns at low supercriticalities almost do not differ from that of the subcritical steady state (Fig. 1), at least up to $Gr = 3.4 \times 10^6$, as is illustrated in the Animations 1 and 2. In both cases, the flow oscillations are noticeable for the potentials Ψ_y that describes the main convective circulation and Ψ_x. For comparison, patterns of Ψ_y of unstable steady states at $Gr = 3.4 \times 10^6$ are shown in Fig. 4. We observe that circulating flow around the cavity persists only near the sidewalls, while in the central part motion in the (x, z) planes becomes quite complicated. In the two cases considered, it differs in the central part of the cube, but this difference is mostly a result of different steady-state flow patterns. Examining oscillations of the potential Ψ_x describing motion in (y, z) planes, we observe that it remains almost unchanged in the CC–CC case, while oscillates noticeably in the CC–AA case.

Trying to follow development of supercritical oscillatory regimes at larger Grashof numbers, we observe that in the CC–CC case the oscillations take place with a single frequency, closed to the one reported in Table 3 and its harmonics. In the CC–AA case, the oscillatory regime becomes unstable already at $Gr = 3.4 \times 10^6$, and transforms into a multi-frequent regime with at least five dominating frequencies.

5.2 AA–CC case

In the AA–CC case, starting from the 150^3 grid, we observe oscillations with a low dimensionless frequency, $f_{\rm cr} \approx 0.01$ that appear at $Gr_{\rm cr} \approx 1.2 \times 10^8$. The calculations in this case, as well as in the next AA–AA case, are much more computationally demanding, not only because of the noticeably larger Grashof number, but also because of low-frequency oscillations that require very long computational times to arrive to an asymptotic oscillatory regime. Since all previous studies for thermally insulated horizontal boundaries were done for the AA–AA case only, no independent data are available for comparison. It is stressed again that calculations on a coarser 100^3 grid resulted in oscillations with a quite different frequency, and also showed different transitional time histories from those discussed below.

Time histories of the total kinetic energy at slightly sub- and supercritical Grashof numbers are shown in Fig. 5. Being in the subcritical regime, at $Gr = 1.1 \times 10^8$ and 1.2×10^8, we observe several decaying irregular oscillations, that after some time, result in single-frequency oscillations with decaying amplitude. After the Grashof number is increased beyond the critical one, the initial irregular oscillations transform into a many-frequent periodic regime containing the main frequency and its three to five harmonics. A regular transient part of this transition lasts only 3–4 periods, so that we were unable to extract growth rates from these signals. The critical values reported in Table 2 are obtained by extrapolation of decay rates to zero, and the frequencies reported in Table 3 are taken from the decaying time histories. The oscillations pertain for a long time, about 20–30 oscillation periods, without any evidence of instability of this limit cycle. The amplitude of oscillations remains relatively small, so that the Nusselt number and the total kinetic energy of the time-averaged and unstable steady flow at $Gr = 1.3 \times 10^8$ differ only in the third decimal place. Reduction in the Grashof number from 1.3×10^8 to 1.25×10^8 resulted in a steady-state flow. Thus, we can assume that this is a supercritical bifurcation into a many-frequent limit cycle.

The transition observed breaks both rotation and 2D reflection symmetries, but sustains the centro-symmetry of the flow. Thus, examination of the temperature distribution in a certain snapshot shows that the maximal

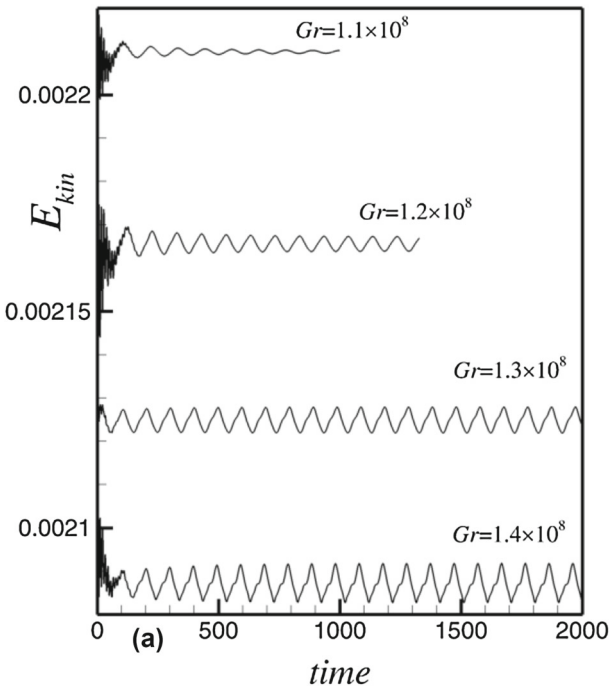

Fig. 5 Time evolution of the total kinetic energy at $Gr = 1.1 \times 10^8$ to $Gr = 1.4 \times 10^8$ for the AA–CC case. Calculation on the 150^3 grid

absolute deviation between $\theta\,(x, y, z)$ and either of $\theta\,(x, 1-y, z)$ or $-\theta\,(1-x, y, 1-z)$ is exactly 0.0632. The maximal absolute deviation between $\theta\,(x, y, z)$ and $\theta\,(1-x, 1-y, 1-z)$ is $1.9{\cdot}10^{-7}$. Here, we observe the exceptional case described in Sect. 2.

A pattern of the temperature amplitude in a slightly oscillatory regime at $Gr = 1.3 \times 10^8$ is shown in Fig. 6. The amplitude isosurfaces (Fig. 6) form many small-scale structures that conceal most of its important properties. To get more insight, the amplitude isolines are plotted in characteristic cross sections by the coordinate planes (Fig. 6b–d). We observe that there are no intensive temperature oscillations in the central part of the box. The maximal amplitude values (red color) are located near all the six box borders, namely (1) near the spanwise boundaries $y = 0$ and 1 in the corners $x = z = 1$ and $x = z = 0$, respectively (Fig. 6b); (2) near the isothermal boundaries $x = 0$ and 1 in the corners $y = z = 0$ and $y = z = 1$, respectively (Fig. 6c); and (3) in the upper and lower parts of the cavity inside the boundary layers adjacent to the vertical boundaries (Fig. 6d). Clearly, such an amplitude pattern cannot be directly compared to a 2D result for the AA square cavity (see below), since the similarity, if any, is expected to be observed in the midplane $y = 0.5$. We conclude that the oscillations observed have a fully three-dimensional origin.

Comparison of the potential isosurfaces of unstable steady-state and time-averaged flow (Fig. 7) at $Gr = 1.3 \times 10^8$ does not reveal any noticeable qualitative changes in the potentials Ψ_y and Ψ_x. The potential Ψ_z changes noticeably in the central part of the box. This change is illustrated additionally by arrow plots in the $z = \text{const}$ planes where we observe a break of reflection symmetry of vortical motion in the (x, y) planes, which is caused by oscillations of the z-component of vorticity. We observe also the fastest convective motion along the main circulation (left frames) shifted toward the spanwise boundaries. Comparing maximal values of the vortex potentials, we notice also that in the time-averaged flow, the main circulation slightly weakens, compared to the steady-state one, while the motion in the two remaining coordinate planes slightly intensifies. The snapshots of the oscillations (not shown in the figures) reveal that the most noticeable oscillations are located in the central part of the cube, while the motion remains fastest near the spanwise boundaries.

5.3 AA–AA case

This case appears to be the most difficult for computational simulation. Previous computations performed on coarser grids reported transition to unsteadiness at the Grashof number between 4×10^7 and 5×10^7

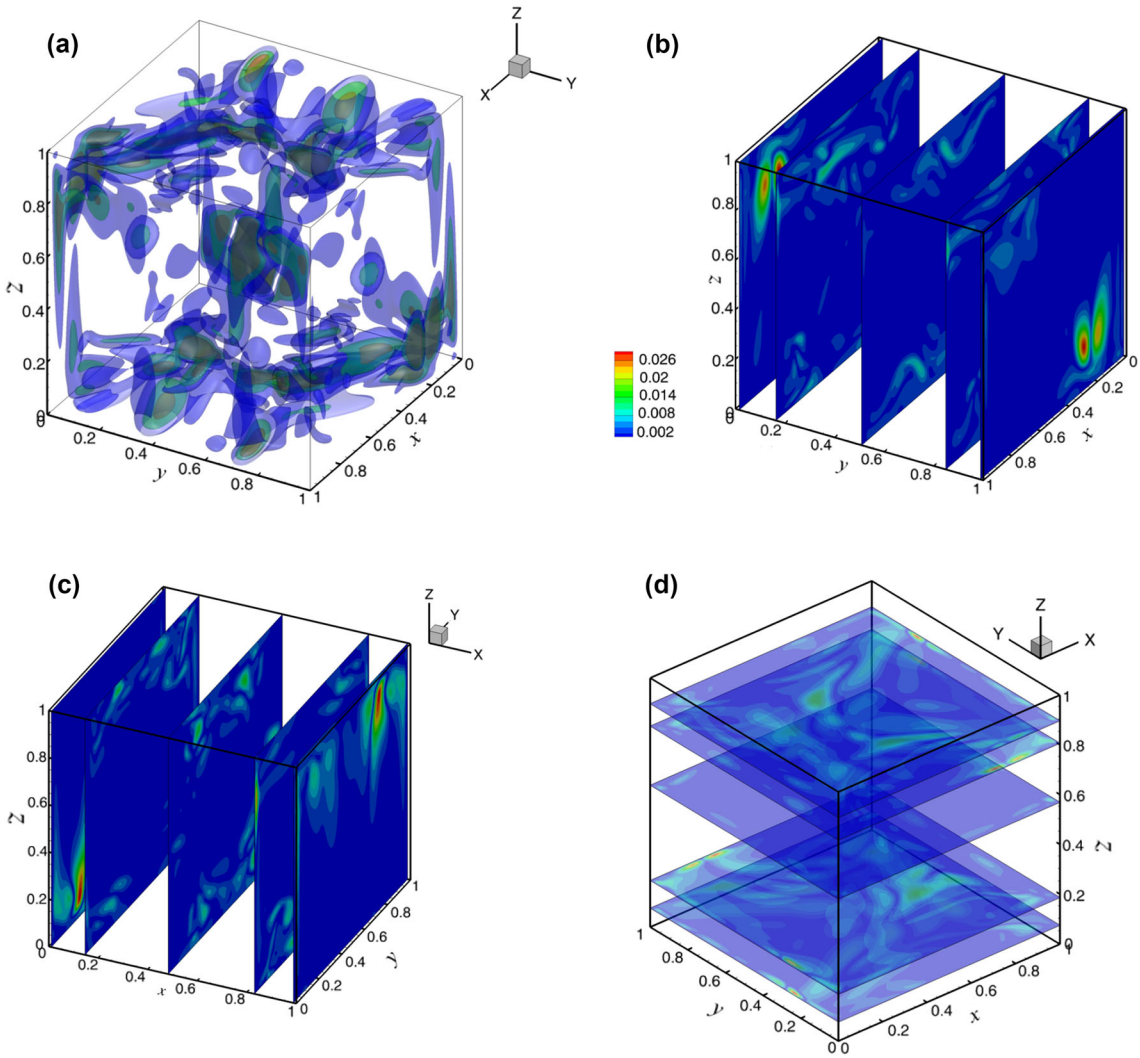

Fig. 6 **a** Isosurfaces of amplitude of temperature oscillations at $Gr = 1.3 \times 10^8$ in the AA–CC case. The maximal value and levels plotted are 0.0302, 0.004, 0.007, 0.01. **b–d** Amplitude isolines in characteristic y-, x-, and z-cross sections, respectively. Calculation on the 200^3 grid. Animation 3

(Table 2). At the same time the our previous computations on the 100^3 grid [24] arrived to a steady flow at $Ra = GrPr = 10^8$, which was verified here by calculations performed on the three finer grids, and agrees with the result of [20]. To resolve this apparent contradiction, we needed to perform a series of very careful CPU-time consuming computations varying the Grashof number from 4×10^7 to 3×10^8. The steady-state flow patterns of this case were already reported in [24], and are not shown here.

The first steady–oscillatory transition was found to take place at $Gr_{\rm cr}^{(1)} \approx 4.6 \times 10^7$ with breaking of all the three symmetries. The characteristic time dependence of the total kinetic energy and the Nusselt number is shown in Fig. 8. The calculations start from the steady state at $Gr = 4.55 \times 10^7$. An abrupt increase in the Grashof number to 4.6×10^7 results in irregular large amplitude oscillations that are attributed to non-modal disturbances growth mechanism. These oscillations decay in a relatively short time, after which the flow remains almost unchangeable during ≈500 time units, so that the pointwise relative difference between the two time steps becomes of the order of 10^{-7}. The latter can be mistakenly interpreted as a steady state. As mentioned above, to ensure that the computations converge to a steady state (e.g., at $Gr = 4.5 \times 10^7$), and to distinguish it from a slowly developing transient regime, the computational process was terminated only after the pointwise relative difference between two consecutive time steps was below 10^{-9}. After a long transient period, the amplitude starts to grow, and finally the computational process arrives to an oscillatory flow

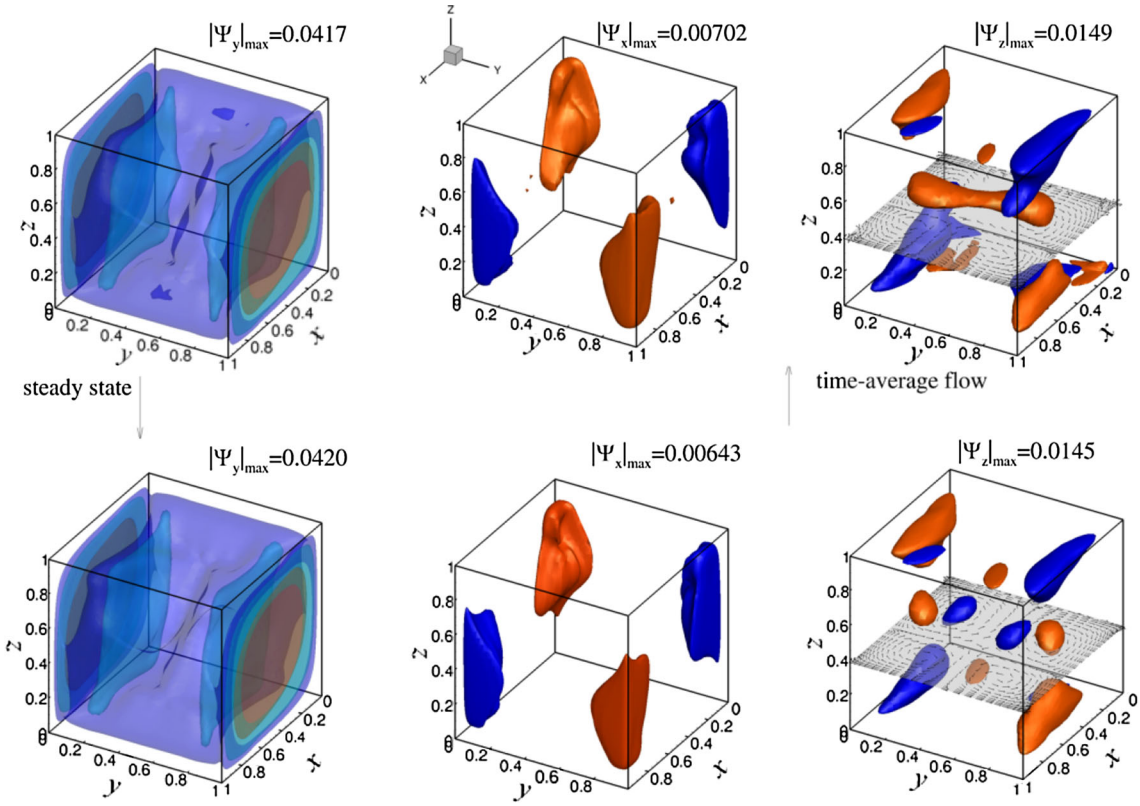

Fig. 7 Comparison of vector potentials of the time-averaged oscillatory flow states at $Gr = 1.3 \times 10^8$ in the AA–CC (*upper frames*) with those of the unstable steady state at the same Grashof number (*lower frames*). Isosurface are shown at $\Psi_y = 0.006$, 0.01 and 0.02, $\Psi_x = \pm 0.004$, and $\Psi_z = \pm 0.004$. Calculation on the 200^3 grid

regime. The spectrum of the oscillations shown in the insert of Fig. 8 contains the main frequency $f \approx 0.01$, its harmonics and a sub-harmonic. Clearly, much longer time integration is needed to reach a definite conclusion about the asymptotic oscillatory state.

A long transient time needed for the instability development can be connected to the symmetry breaking. Since the initial state is symmetric, no non-symmetric perturbations are introduced. The numerical growth of these perturbations starts from the round-off errors and may consume a long integration time until arriving to a noticeable amplitude that still remains relatively small compared to other cases considered. Note that similar calculations in [16] resulted in the break of only reflection symmetry with a preserved rotational one. Possibly, in these calculations, the break of rotational symmetry was not resolved, which resulted in a critical Grashof number larger than the one computed here.

The calculations performed for $Gr = 4.55 \times 10^7$ resulted in a steady state when they were started from the steady flow at $Gr = 4.5 \times 10^7$. When the oscillatory state at $Gr = 4.6 \times 10^7$ was taken as an initial condition, the computations at $Gr = 4.55 \times 10^7$ arrived to an oscillatory flow. This indicates on the subcritical steady–oscillatory transition.

The second transition occurs when the Grashof number crosses the second critical value $Gr_{\rm cr}^{(2)} \approx 7.1 \times 10^7$. With the increase in the Grashof number already to $Gr = 7.15 \times 10^7$ the oscillatory flow turns into a stable and steady one with all the symmetries reinstated. Figure 9 illustrates destabilization of the flow with the decrease of the Grashof number from 7.2×10^7 to 7.0×10^7. We observe that being steady and stable at $Gr = 7.15 \times 10^7$, the flow becomes unstable at $Gr = 7.1 \times 10^7$. Computations at $Gr = 7 \times 10^7$ and $Gr = 7.1 \times 10^7$ (Fig. 9) exhibit first quasi-steady and then quasi-regular oscillatory time dependencies. At longer times the oscillations become irregular. Significantly longer time integration is needed to reach a conclusion about stochastic properties of their asymptotic states, which is beyond the scope of the present study.

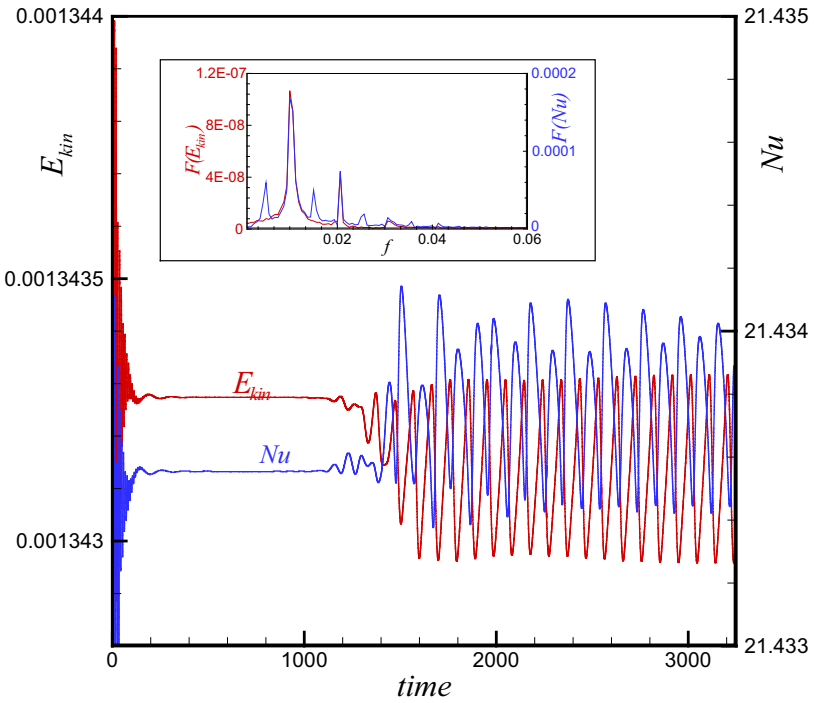

Fig. 8 Time evolution of the total kinetic energy and Nusselt number at $Gr = 4.6 \times 10^7$ starting from steady state at $Gr = 4.55 \times 10^7$ in the AA–AA case. The *inset* shows the frequency spectra of both time dependencies calculation for $2000 < t < 3000$. Calculation on the 200^3 grid

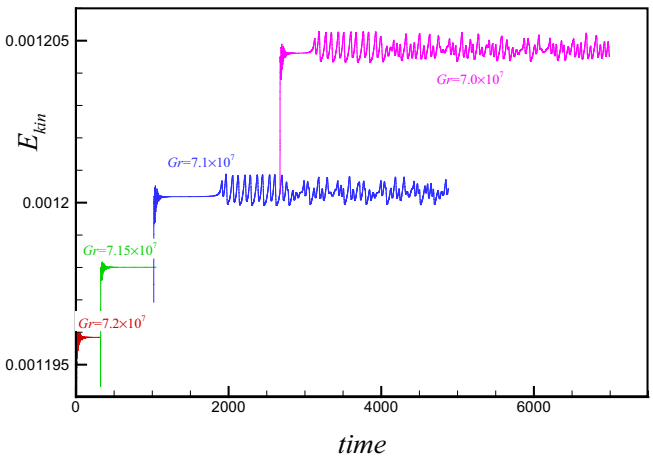

Fig. 9 Time evolution of the total kinetic energy from $Gr = 7.2 \times 10^7$ up to $Gr = 7.0 \times 10^7$ starting from steady state at $Gr = 7.25 \times 10^7$ in the AA–AA case. Calculation on the 200^3 grid

The restored stable steady states remain stable up to $Gr_{\rm cr}^{(3)} \approx 2.8 \times 10^8$. As is shown in Figs. 10 and 11, the oscillations at $Gr = 2.7 \times 10^8$ slowly decay, while at $Gr = 2.8 \times 10^8$ the time dependencies become more complicated. At the transitional stage, we observe decaying low-frequency oscillations that are modulated by larger frequency ones. The spectrum of these oscillations, plotted in the insert of Fig. 10, shows that the two frequencies differ in more than an order of magnitude. Finally, only large frequency oscillations with very small amplitude remain. By gradually increasing the Grashof number, we observe that the oscillation amplitude slowly grows, as is expected (Fig. 11). The lower frequency, that modulates the larger-frequency time dependence (Fig. 10), varies from 0.043 at $Gr = 2.8 \times 10^8$ to 0.090 at $Gr = 3 \times 10^8$. This transition preserves the three symmetries that start to break already at $Gr \approx 2.9 \times 10^8$. This time behavior was observed for 150^3, 200^3, and 256^3 grids.

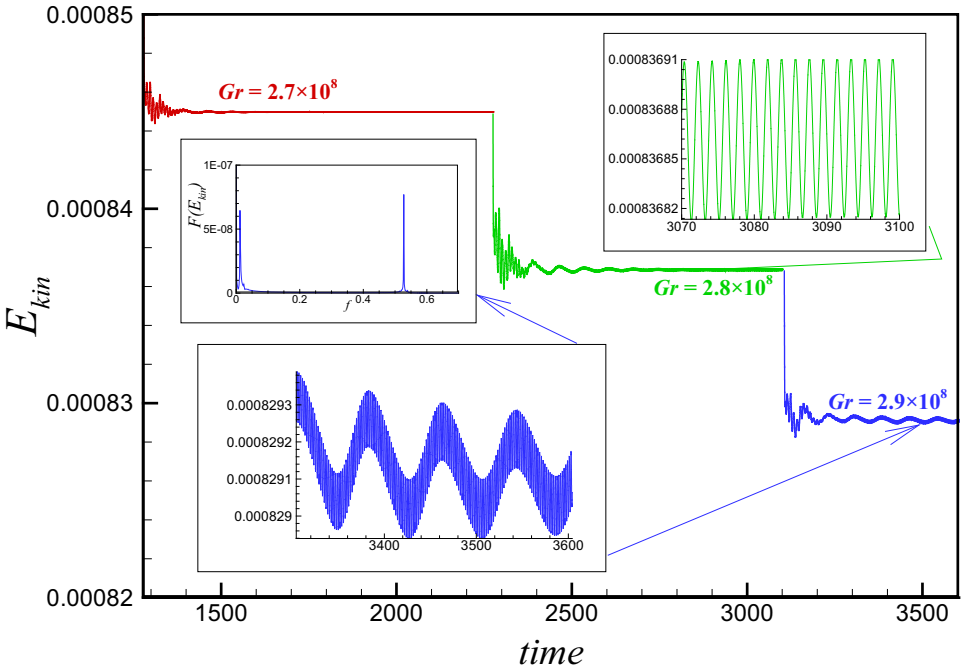

Fig. 10 Time evolution of the total kinetic energy from $Gr = 2.6 \times 10^8$ to $Gr = 2.7 \times 10^8$ (*red line*), then to $Gr = 2.8 \times 10^8$ (*green line*), and then to $Gr = 2.9 \times 10^8$ (*blue line*). The AA–AA case. Calculation on the 200^3 grid (color figure online)

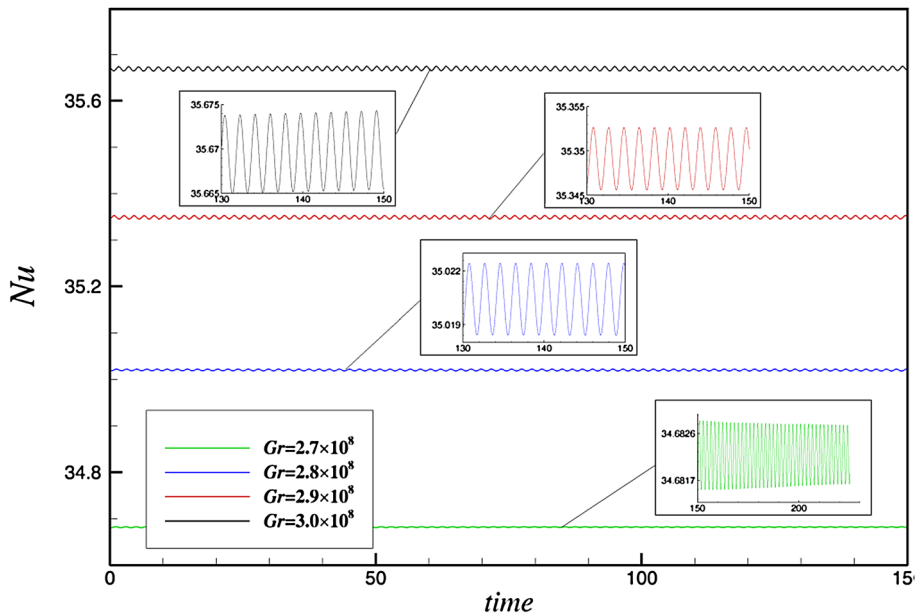

Fig. 11 Large-frequency/small-amplitude oscillations of the Nusselt number computed for gradually increased Grashof number in the AA–AA case. Calculation on the 200^3 grid

As follows from Table 2, calculations on the 100^3 grid for the AA–AA case fail to predict either a correct critical Grashof number, or correct frequency of oscillations, or both. A similar conclusion can be made when current fine grid results are compared with the previous studies performed on coarser grids. Thus, critical Grashof numbers and oscillation frequencies reported in [16,17,19] coincide with the present result for the first bifurcation, as well as between themselves, only in the first decimal place. Results of [18,20] differ drastically from the above cited ones, and possibly relate to the third transition reported here. Their critical

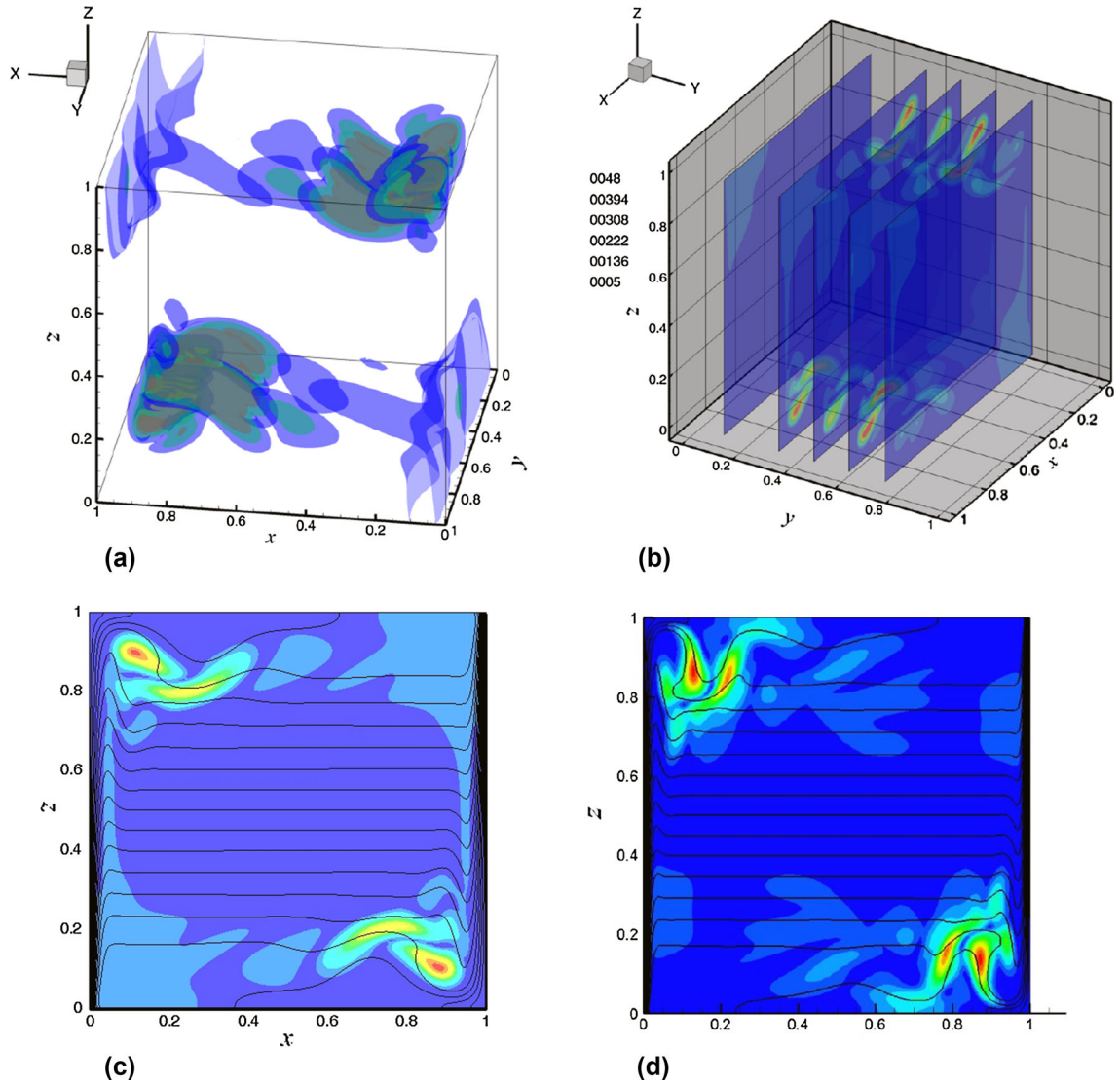

Fig. 12 **a** Isosurfaces of amplitude of temperature oscillations at $Gr = 4.7 \times 10^7$ in AA–AA case. **b** Amplitude of the temperature oscillations in several $y = \text{const}$ planes of the frame **a**. **c** Isotherms (*black lines*) and amplitude of the temperature oscillations (*colors*) in $y = 0.5$ plane of the frame **a**. **d** Isotherms (*black lines*) and amplitude of the temperature oscillations (*colors*) of the most unstable perturbation in the 2D AA case. Calculation on the 150^3 grid. Animation 4 (color figure online)

Grashof numbers are of the same order of magnitude as our $Gr_{\text{cr}}^{(3)}$. The frequency reported in [20] is 0.532, which is close to the present result. The dimensionless frequency obtained in [18] and scaled by H^2/α, is 0.43. If it is rescaled by $Pr/\sqrt{Gr}$ to be compared with the present results, it becomes surprisingly small.

Amplitude of the temperature oscillations after the first transition at $Gr_{\text{cr}}^{(1)} \approx 4.6 \times 10^7$ is shown in Fig. 12a–c and is compared with the most unstable temperature perturbation in the 2D cavity with perfectly insulated horizontal boundaries (AA cavity). We observe a sharp maxima of the amplitude in the lower right and upper left corners, with a much weaker maxima in the opposite corners (Fig. 12a). Some more insight can be gained also from the cross-sectional plots in Fig. 12b. Since the large amplitude values are located near the midplane $y = 0.5$ and the global maxima lay in the midplane, we can compare the pattern with the most unstable perturbation of the corresponding 2D instability in the square cavity. Thus, comparing Fig. 12c, d we observe that the maxima of both cases are located in the same corners; however, patterns of the amplitudes noticeably differ. Taking into account that steady–oscillatory transition in the 2D case takes place at a significantly larger Grashof number, $Gr \approx 2.6 \times 10^8$, we can state only partial similarity of the 2D and 3D instabilities. Stability of the 2D flow in a square cavity with respect to spanwise-periodic three-dimensional perturbations was studied

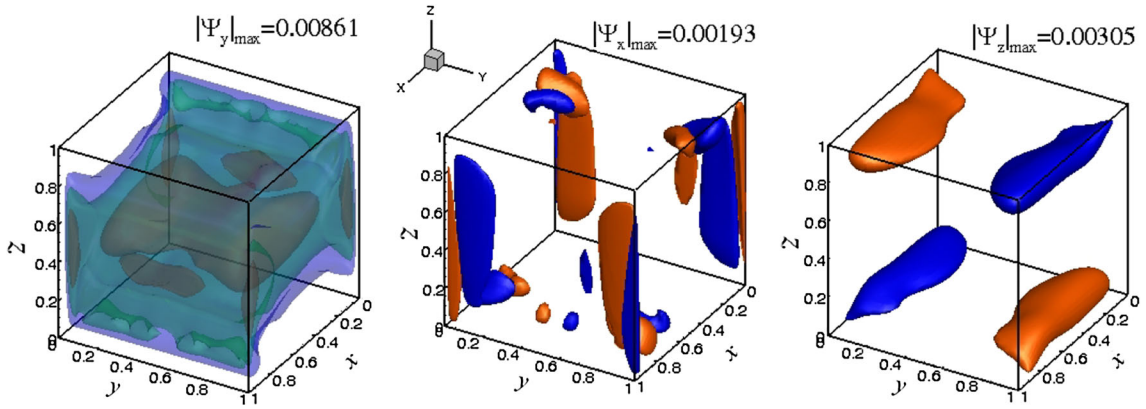

Fig. 13 Time-averaged flow at $Gr = 7 \times 10^7$ in the AA–AA case. Isosurface are shown at $\Psi_y = 0.0045$, 0.006 and 0.0075, $\Psi_x = \pm 0.0006$, and $\Psi_z = \pm 0.001$. Calculation on the 200^3 grid

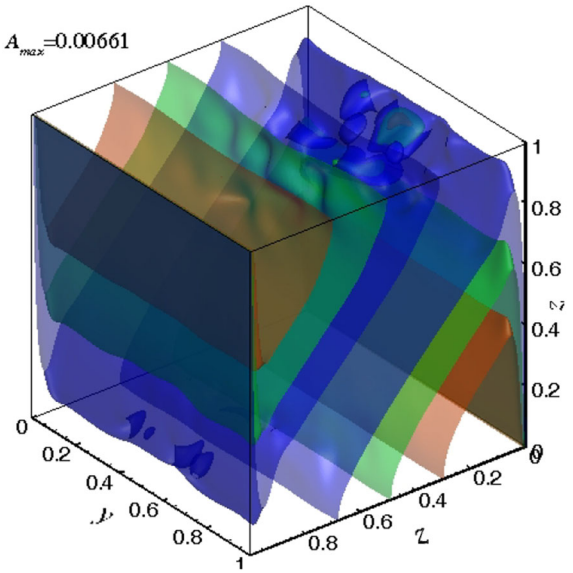

Fig. 14 Amplitude of the lowest frequency of the three-frequent temperature oscillations at $Gr = 7 \times 10^7$, AA–AA case. Calculation on the 200^3 grid

in [23]. The transition from steady 2D to steady 3D flow was found at $Gr = 2.18 \times 10^7$, which is a completely different result compared to the present one. Nevertheless, the temperature perturbation shown in Figure 1 of [23] exhibits some similarity to the one shown in Fig. 12a of this paper.

Due to the small oscillation amplitude, the time-averaged and steady-state flow patterns look undistinguishable and are not shown. As previously stated, based on this small difference, we assume that the bifurcation is supercritical. The oscillations consist of weak pulsations of the main convective vortex (potential Ψ_y), and stronger oscillations in two other coordinate planes (potentials Ψ_z and Ψ_x), as is seen from the animation at $Gr = 5 \times 10^7$ attached to Fig. 8.

The Fourier analysis of the time dependencies slightly below the second oscillatory–steady transition (Fig. 9) shows three frequency peaks for dimensionless frequencies 0.00610, 0.0122, and 0.0183, with the largest peak corresponding to the second value. It is not clear whether the two larger frequencies are harmonics of the lower one, or the lower one results from a period doubling of the second frequency. The time-averaged flow calculated at $Gr = 7 \times 10^7$ and shown in Fig. 13 is very close to the corresponding unstable steady state. As stated above, this indicates on a smooth transition from the steady to oscillatory regime, with the decrease of the Grashof number. Amplitudes of all the three frequencies have a similar pattern, so that only one of them is shown in Fig. 14. These patterns are qualitatively different from the one observed at the first

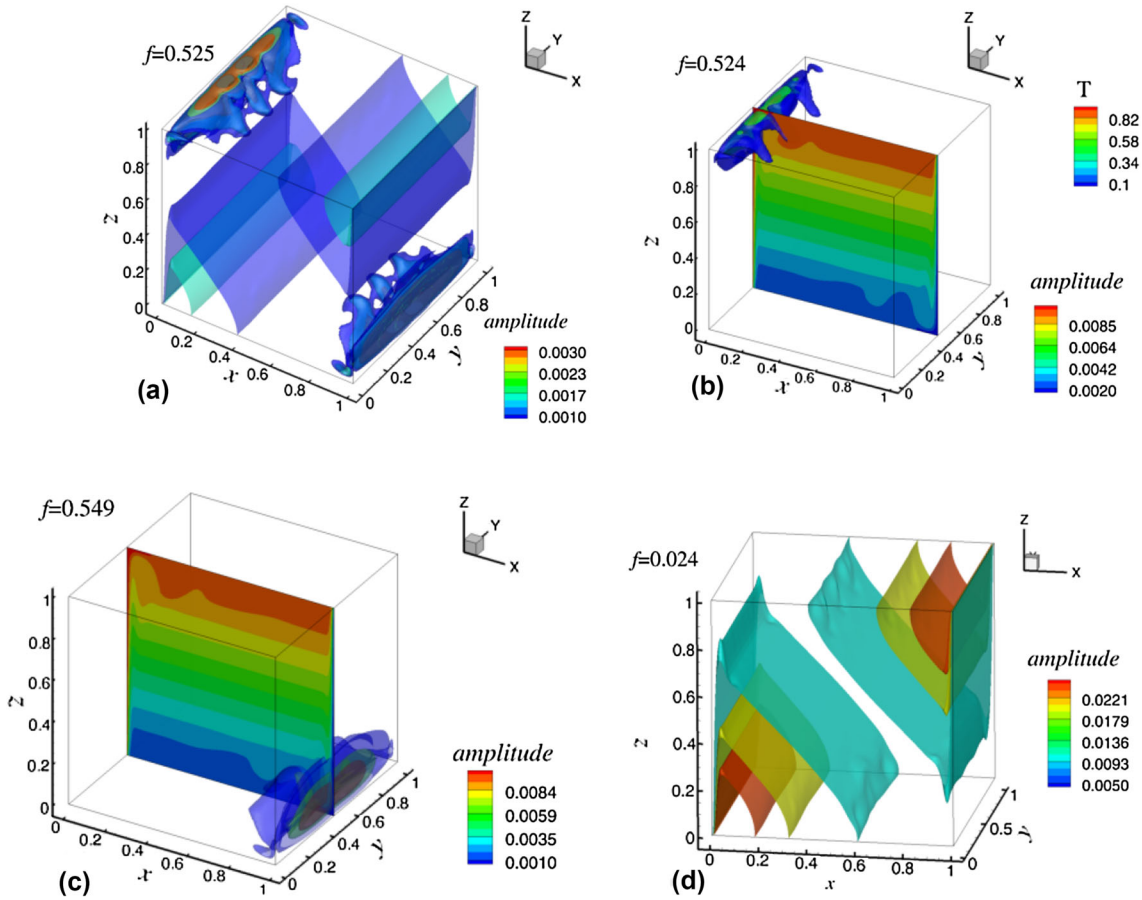

Fig. 15 Amplitudes of temperature oscillations at $Gr = 2.9 \times 10^8$, the AA–AA case. **a** Amplitude of the single-frequency regime shown in this figure. **b–d** Amplitudes of the three main frequencies of the second oscillatory regime. Calculation on the 150^3 grid

transition (Fig. 12). Recalling the linear stability analysis, the similarity indicates again that the oscillations at all the three frequencies result from the same eigenmode of the linearized problem.

When the Grashof number is increased slightly above 2.8×10^8, we observe the appearance of two-frequency oscillations (Fig. 10). As mentioned above, integration over a longer time leads to a decay of the lower frequency oscillations, so that only low-amplitude and large-frequency oscillations sustain, as is shown in Fig. 11. The characteristic frequency of these oscillations is 0.525 (Table 3). This regime remained stable and preserved all the symmetries for long integration times when computations were performed on the 200^3 and 256^3 grids. When the calculations started from the developed oscillatory regime at $Gr = 2.8 \times 10^8$ and the Grashof number was reduced to $Gr = 2.7 \times 10^8$, the oscillatory regime sustained, from which we concluded that the observed instability is subcritical.

Due to the very small amplitude the time-average and unstable steady flow regimes are very close and look undistinguishable on a graph (not shown here). The amplitude of the temperature oscillations of this regime is shown in Fig. 15a. Its pattern can be seen as a superposition of the patterns resulting from the two previous transitions (Figs. 12, 17). We observe that the largest amplitudes are located inside rotation-symmetric small-scale structures in the lower right and the upper left corners, which is similar to the pattern of the first transition (Fig. 12). Two other rotation-symmetric structures with smaller amplitudes start from the opposite corners and propagate deeper into the flow, similarly to the amplitude patterns of the second transition (Fig. 14).

Computations on the 150^3 grid at $Gr = 2.9 \times 10^8$, starting from a snapshot at $Gr = 2.8 \times 10^8$, arrived to the above described two-frequency regime, which became unstable, and after a longer time integration, resulted in another oscillatory regime with all the symmetries broken. The corresponding history of the total kinetic energy and the Nusselt number is shown in Fig. 16. The new (second) oscillatory regime is characterized by three frequencies 0.024, 0.524, and 0.549 clearly seen in the Fourier spectrum. Using an interpolated snapshot of this regime as an initial state for calculation on finer grids shows that it pertains almost unchanged, as is

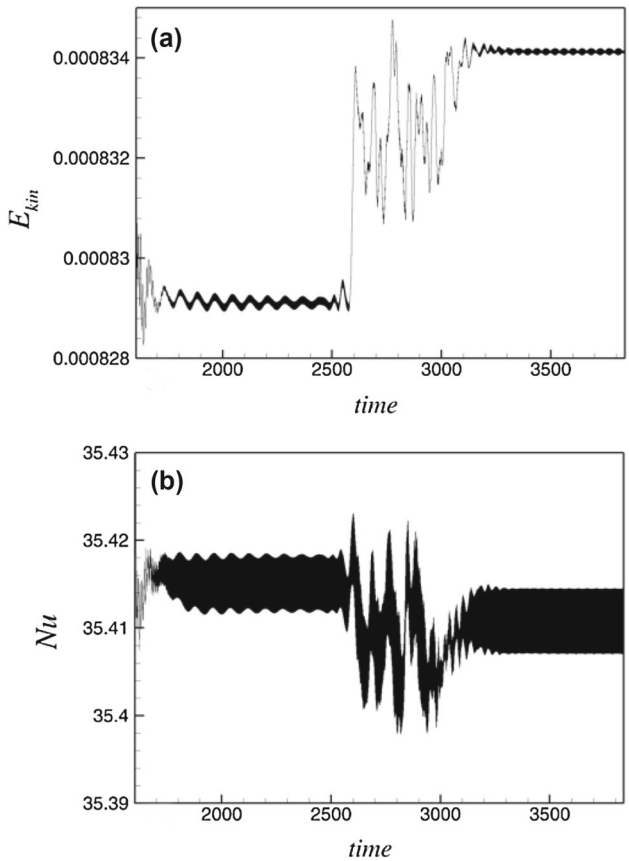

Fig. 16 Time evolution of the total kinetic energy (**a**) and Nusselt number (**b**) at $Gr = 2.9 \times 10^8$. The AA–AA case. Calculation on the 150^3 grid

shown in Fig. 2b for $Gr = 3 \times 10^8$. When the Grashof number is increased to 3×10^8, the lowest frequency remains the same, while the two larger frequencies change to 0.528 and 0.553.

We tried to reproduce the instability of the single-frequency oscillatory regime, as is shown in Fig. 16, calculating on the two finer grids, and succeeded to observe it on the 200^3 grid at $Gr = 3 \times 10^8$. On the 256^3 grid, the large-frequency regime did not exhibit any instability for a very long integration time. Thus, it remains unclear whether the instability sets in at even a more longer time, or at a larger Grashof number, or two oscillatory regimes become separated at finer grids. Further, we performed calculations on the 150^3 and 200^3 grids gradually reducing the Grashof number by decrements of 10^7. Oscillations corresponding to the second oscillatory regime sustains up to $Gr = 2.3 \times 10^8$, where the flow oscillates with the main frequency 0.03 and its harmonics.

To illustrate these oscillatory regimes by animation or snapshots is rather difficult since either the amplitude is too small, or too many frames are needed to be stored or plotted. Some additional information can be derived from the spatial distribution of the frequencies amplitude and time-averaged flow pattern. Thus, Fig. 15 compares spatial distribution of the oscillation amplitude of the primary large-frequency oscillations (Fig. 15a) with those of the three frequencies found in the spectrum of the second oscillatory regime (Fig. 15b–d). A rather surprising observation is that in the amplitude, structures that appeared together in the single-frequency regime become separated, and each of them oscillates with its own frequency. This separation can be connected with the observed symmetry breaking.

To compare the 2D and 3D cases also for this transition, the amplitude of 3D temperature oscillations is plotted in several $y = \text{const}$ cross sections, together with the time-averaged isotherms. It is seen that the 3D amplitude is noticeably larger near the midplane $y = 0.5$, which would indicate on some analogy with the 2D case. However, the shape of the 3D amplitude pattern is not similar to its 2D counterpart and is located "deeper" in the corners (cf. Figs. 12b, 17). Also, the presence of large (but not largest) amplitude oscillations

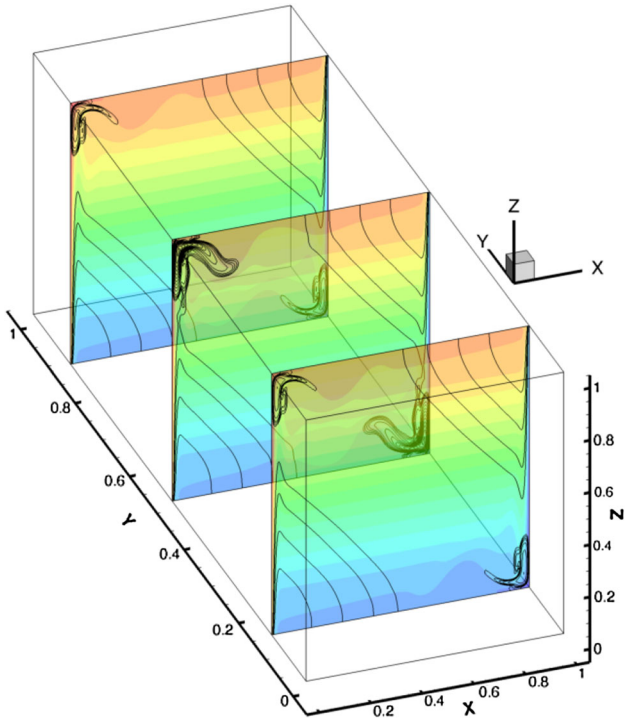

Fig. 17 Time-averaged isotherms (*colors*) and amplitude of the single-frequency oscillatory regime at $Gr = 2.9 \times 10^8$, the AA–AA case. Calculation on the 150^3 grid (color figure online)

propagating from the lower left and upper right corners in the bulk of the flow indicates a different, compared to the 2D case, origin of the instability.

6 Conclusions and discussion

Steady–oscillatory transition and slightly supercritical oscillatory states of buoyancy convection in a laterally heated cube were studied by the straight-forward time integration of Bousinesq equations. Pressure/velocity segregated and coupled time-integration schemes were applied. Four different sets of thermal boundary conditions were taken into consideration. Either perfectly thermally conducting (CC) or perfectly thermally insulated (AA) horizontal and spanwise boundaries were considered. Special attention was paid to the grid convergence of the results. Three-dimensional velocity fields are visualized using a novel approach of quasi-two-dimensional divergence-free projections [24,25]. The obtained values of the critical Grashof numbers and critical oscillation frequencies comprise a set of benchmark data needed for validation of future numerical methods that will allow one to solve fully three-dimensional (TriGlobal) stability problems. The results for the AA–AA and AA–CC cases are new. The second and third transitions in the AA–AA case are quite unexpected and have never been reported. The results for the CC–AA case and for the primary bifurcation in the AA–AA case, noticeably improve accuracy of the previous studies.

When cube horizontal boundaries are perfectly thermally conducting (the CC–CC and CC–AA cases), the steady–oscillatory transition takes place at $Gr \approx 3.3 \times 10^6$, which, together with the calculated oscillation frequencies, agree well with the previous findings of [14,15], and is not far from the experimentally measured values of [13]. The critical Grashof numbers and the oscillations frequency are also close to those obtained for convection in a laterally heated two-dimensional square cavity [7,22]. We showed also that the amplitude of the most unstable two-dimensional perturbation, resulting from the linear stability analysis, is similar to the three-dimensional pattern of the oscillation amplitude. These allows us to argue that in the case of perfectly conducting horizontal walls, the two- and three-dimensional instabilities set in similarly, and support the argument made in [14,15], that this instability is driven by local Rayleigh-Bénard mechanisms. In both cases the steady–oscillatory transitions are supercritical. At the same time, in spite of the similar instability mechanism, the two bifurcations differ with respect to the symmetry breaking: in the CC–CC case the reflection

symmetry is preserved, while in the CC–AA case all the symmetries are broken. Consequently, further flow changes, even at small supercriticalities, differ qualitatively.

When the horizontal boundaries are perfectly thermally insulated (the AA–CC and AA–AA cases), the primary bifurcation takes place at Grashof numbers that are more than an order of magnitude larger than those obtained for the perfectly insulated horizontal boundaries. Also, both oscillation amplitude and frequency become about an order of magnitude smaller, which cause additional numerical difficulties. It was observed that the primary steady–oscillatory transition is qualitatively different for perfectly thermally conducting (AA–CC) and perfectly insulated (AA–AA) spanwise walls. Furthermore, this transition breaks rotation and 2D reflection symmetries, but remains symmetric with respect to their superposition, which is considered as a rare and exceptional case.

In the AA–CC case, the critical Grashof number is found to be beyond 1.2×10^8, and oscillations appear with a relatively low dimensionless frequency ≈ 0.01. The transition from the steady to oscillatory regime is supercritical. No independent numerical or experimental data are available here for comparison. The instability observed does not exhibit any similarities with the corresponding 2D AA case.

In the AA–AA case, three consecutive steady–oscillatory transitions were observed and two of them are reported here for the first time. The first one takes place at $Gr \approx 4.6 \times 10^7$ with the break of all the symmetries and via a subcritical bifurcation. The critical Grashof number and oscillation frequency are close to previously reported values [17–19] and are converged to within the second decimal digit. The transition breaks all the symmetries of the base flow and exhibits some partial similarities with the analogous 2D case. At $Gr \approx 7.2 \times 10^7$, the stability of steady states restores together with all the symmetries. We presented some arguments showing that this transition is supercritical with respect to the decreasing Grashof number. Finally, at $Gr \approx 2.8 \times 10^8$ the steady flow becomes unstable sustaining the symmetries. There is also some evidence that the resulting single-frequency oscillatory flow becomes unstable again already at $Gr \approx 2.9 \times 10^8$ and transforms into oscillations with three characteristic frequencies and a break of the symmetries. This transition indicates on possible subcriticality, so that single and triple-frequency regimes are observed at the same Grashof numbers.

Returning to the comparison of 3D and 2D results on the steady–oscillatory transition, we conclude that only the CC–CC and CC–AA cases exhibit complete similarity with its two-dimensional CC counterpart. Only partial similarity is observed for the first bifurcation in the AA–AA case, while in the AA–CC case, no similarities were observed.

Acknowledgements This work was supported by the LinkSCEEM-2 project, funded by the European Commission under the 7th Framework Program through Capacities Research Infrastructure, INFRA-2010-1.2.3 Virtual Research Communities, Combination of Collaborative Project and Coordination and Support Actions (CP-CSA) under grant agreement no RI-261600. The author acknowledges PRACE for awarding him access to resource CURIE based in France at Très Grand Centre de Calcul.

References

1. Lappa, M.: Thermal Convection: Patterns, Evolution and Stability. Wiley, Singapore (2010)
2. Gelfgat, AYu., Bar-Yoseph, P.Z., Yarin, A.L.: Stability of multiple steady states of convection in laterally heated cavities. J. Fluid Mech. **388**, 315–334 (1999)
3. Xin, S., Le Quéré, P.: An extended Chebyshev pseudo-spectral benchmark for the 8:1 differentially heated cavity. Int. J. Numer. Methods Fluids **40**, 981–998 (2002)
4. Theofilis, V.: Global linear instability. Ann. Rev. Fluid Mech. **43**, 319–352 (2011)
5. Gómez, F., Le Clainche, S., Paredes, P., Hermanns, M., Theofilis, V.: Four decades of studying global linear instability: problems and challenges. AIAA J. **50**, 2731–2743 (2012)
6. Dijkstra, H.A., Wubs, F.W., Cliffe, A.K., Doedel, E., Dragomirescu, I.F., Eckhardt, B., Gelfgat, A.Y., Hazel, A.L., Lucarini, V., Salinger, A.G., Phipps, E.T., Sanchez-Umbria, J., Schuttelaars, H., Tuckerman, L.S., Thiele, U.: Numerical bifurcation methods and their application to fluid dynamics: analysis beyond simulation. Commun. Comput. Phys. **15**, 1–45 (2013)
7. Xin, S., Le Quéré, P.: Linear stability analyses of natural convection flows in a differentially heated square cavity with conducting horizontal walls. Phys. Fluids **13**, 2529–2542 (2001)
8. Feldman, Y., Gelfgat, AYu.: Oscillatory instability of a 3D lid-driven flow in a cube. Phys. Fluids **22**, 093602 (2010)
9. Kuhlmann, H.C., Albensoeder, S.: Stability of the steady three-dimensional lid-driven flow in acube and the supercritical flow dynamics. Phys. Fluids **26**, 024104 (2014)
10. Anupindi, K., Lai, W., Frankel, S.: Characterization of oscillatory instability in lid driven cavity flows using lattice Boltzmann method. Comput. Fluids **92**, 7–21 (2014)
11. Gómez, F., Gómez, R., Theofilis, V.: On three-dimensional global linear instability analysis of flows with standard aerodynamics codes. Aerosp. Sci. Technol. **32**, 223–234 (2014)
12. Liberzon, A., Feldman, Y., Gelfgat, AYu.: Experimental observation of the steady-oscillatory transition in a cubic lid-driven cavity. Phys. Fluids **23**, 084106 (2011)

13. Jones, D.N., Briggs, D.G.: Periodic two-dimensional cavity flow: effect of linear horizontal thermal boundary condition. J. Heat Transf. **111**, 86–91 (1989)
14. Janssen, R.J.A., Henkes, R.A.W.M., Hoogendoorn, C.J.: Transition to time-periodicity of a natural convection flow in a 3D differentially heated cavity. Int. J. Heat Mass Transf. **36**, 2927–2940 (1993)
15. Janssen, R.J.A., Henkes, R.A.W.M.: The first instability mechanism in differentially heated cavities with conducting horizontal walls. J. Heat Transf. **117**, 626–633 (1995)
16. Labrosse, G., Tric, E., Khallouf, H., Betrouni, M.: A direct (pseudo-spectral) solver of the 2D/3D Stokes problem: transition to unsteadiness of natural-convection flow in a differentially heated cubical cavity. Numer. Heat Transf. Pt. B **31**, 261–276 (1997)
17. De Gassowski, G., Xin, S., Daube, O., Fraigneau, Y.: Bifurcations and multiple solutions in an air-filled differentially heated cubic cavity. In: Proceedings of International Heat Transfer Conference 13, Begel House Inc. (2006). doi:10.1615/IHTC13.p1.50
18. Sheu, T.W.-H., Lin, R.-K.: Three-dimensional bifurcations in a cubic cavity due to buoyancy-driven natural convection. Int. J. Heat Mass Transf. **54**, 447–467 (2011)
19. Soucasse, L., Riviére, Ph, Soufani, A., Xin, S., Le Quéré, P.: Transitional regimes of natural convection in a differentially heated cubical cavity under the effects of wall and molecular gas radiation. Phys. Fluids **26**, 024105 (2014)
20. Janssen, R.J.A., Henkes, R.A.W.M.: Instabilities in three-dimensional differentially-heated cavities with adiabatic horizontal walls. Phys. Fluids **8**, 62–74 (1996)
21. Le Quéré, P., Behnia, M.: From onset of unsteadiness to chaos in a differentially heated square cavity. J. Fluid Mech. **359**, 81–107 (1998)
22. Gelfgat, AYu.: Stability of convective flows in cavities: solution of benchmark problems by a low-order finite volume method. Int. J. Numer. Methods Fluids **53**, 485–506 (2007)
23. Xin, S., Le Quéré, P.: Stability of two-dimensional (2D) natural convection flows in air-filled differentially heated cavities: 2D/3D disturbances. Fluid Dyn. Res. **44**, 031419 (2012)
24. Gelfgat, AYu.: Visualization of three-dimensional incompressible flows by quasi-two-dimensional divergence-free projections. Comput. Fluids **97**, 143–155 (2014)
25. Gelfgat, A.Y.: Visualization of three-dimensional incompressible flows by quasi-two-dimensional divergence-free projections in arbitrary flow regions. Theor. Comput. Fluid Dyn. (to appear) (2016). arXiv: 1508.05603
26. Gulberg, Y., Feldman, Y.: On laminar natural convection inside multi-layered spherical shells. Int. J. Heat Mass Transf. **91**, 908–921 (2015)
27. Roux, B. (ed.): Numerical Simulation of Oscillatory Convection in Low-Pr Fluids: A GAMM Workshop. Notes on Numerical Fluid Mechanics, 27. Vieweg, Braunschweig (1990)
28. Gebhart, B., Jaluria, Y., Mahajan, R.L., Sammakia, B.: Buoyancy-Induced Flows and Transport. Hemisphere Publishing Corp., New York (1988)
29. Gill, A.E.: The boundary-layer regime for convection in a rectangular cavity. J. Fluid Mech. **26**, 515–536 (1966)
30. Henkes, R.A.W.M., Hoogendoorn, C.J.: On the stability of the natural convection flow in a square cavity heated from the side. Appl. Sci. Res. **47**, 195–220 (1990)
31. Feldman, Y.: Direct numerical simulation of transitions and supercritical regimes in confined three-dimensional recirculating flows. PhD Thesis, Tel-Aviv University (2010)
32. Vitoshkin, H., Gelfgat, AYu.: On direct inverse of Stokes, Helmholtz and Laplacian operators in view of time-stepper-based Newton and Arnoldi solvers in incompressible CFD. Commun. Comput. Phys. **14**, 1103–1119 (2013)
33. Guermond, J.L., Shen, J.: Velocity-correction projection methods for incompressible flows. SIAM J. Numer. Anal. **41**, 112–134 (2003)
34. Deville, M.O., Fischer, P.F., Mund, E.H.: High-Order Methods for Incompressible Fluid Flow. Cambridge University Press, Cambridge (2002)
35. Abe, K., Zhang, S.-L., Mitsui, T., Jin, C.-H.: A variant of the Orthomin(2) method for singular linear systems. Numer. Algorithms **36**, 189–202 (2004)
36. Feldman, Y., Gelfgat, AYu.: On pressure–velocity coupled time-integration of incompressible Navier–Stokes equations using direct inversion of Stokes operator or accelerated multigrid technique. Comput. Struct. **87**, 710–720 (2009)
37. Tric, E., Labrosse, G., Betrouni, M.: A first inclusion into the 3D structure of natural convection of air in a differentially heated cavity, from accurate numerical solutions. Int. J. Heat Mass Transf. **43**, 4043–4056 (1999)
38. Bennet, B.A.V., Hsueh, J.: Natural convection in a cubic cavity: implicit numerical solution of two benchmark problems. Numer. Heat Transf. Part A **50**, 99–123 (2006)
39. Peng, Y., Shu, C., Chew, Y.T.: A 3D incompressible thermal Lattice Boltzmann model and its application to simulate natural convection in a cubic cavity. J. Comput. Phys. **193**, 260–274 (2003)
40. Wakashima, S., Saitoh, T.S.: Benchmark solutions for natural convection in a cubic cavity using the high-order time-space method. Int. J Heat Mass Transf. **47**, 853–864 (2004)
41. Hassard, B.D., Kazarinoff, N.D., Wan, Y.H.: Theory and Applications of Hopf Bifurcation. Cambridge University Press, Cambridge (1981)